Receptor-Driven ERK Pulses Reconfigure MAPK Signaling and Enable Persistence of Drug-Adapted BRAF-Mutant Melanoma Cells

As Published: 10.1016/J.CELS.2020.10.002

Publisher: Elsevier BV

Persistent URL: https://hdl.handle.net/1721.1/136137

Version: Final published version: final published article, as it appeared in a journal, conference proceedings, or other formally published context

Cell Systems

Article

Receptor-Driven ERK Pulses Reconfigure MAPK Signaling and Enable Persistence of Drug-Adapted BRAF-Mutant Melanoma Cells

Graphical Abstract

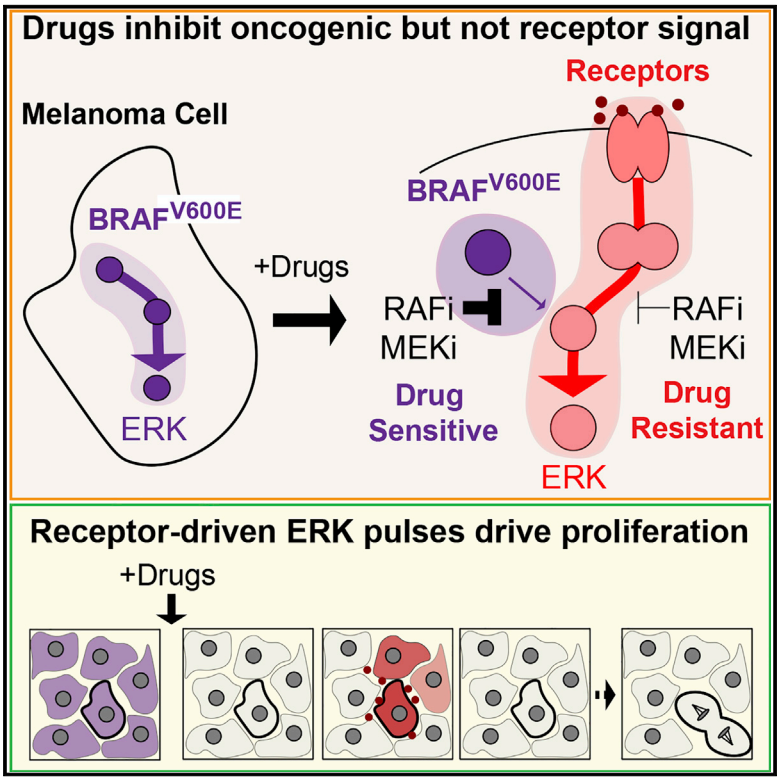

Highlights

- Persister BRAF-mutant melanoma cells emerge during RAF and MEK inhibition
- Persister cells escape cell-cycle arrest via sporadic receptor-driven ERK pulses
- ERK pulses arise spontaneously in neighboring cells via autocrine/paracrine signaling
- Oncogenic vs. receptor-driven MAPK signaling are differentially sensitive to inhibitors

Authors

Luca Gerosa, Christopher Chidley, Fabian Fröhlich, ..., Wei-Jun Qian, H. Steven Wiley, Peter K. Sorger

Correspondence

peter_sorger@hms.harvard.edu

In Brief

Gerosa et al. show that pulsatile MAPK activation makes it possible for slow-growing drug-resistant persisters to emerge when BRAF-mutant melanoma cells are exposed to RAF and MEK inhibitors at clinically relevant doses. Computational modeling shows that MAPK signaling exists in two configurations, one activated by oncogenic BRAF that is drug sensitive and the other activated by autocrine/paracrine growth factors and transmembrane receptors that is drug resistant.

Gerosa et al., 2020, Cell Systems *11*, 478–494
November 18, 2020
https://doi.org/10.1016/j.cels.2020.10.002

CellPress

CellPress
OPEN ACCESS

Cell Systems

Article

Receptor-Driven ERK Pulses Reconfigure MAPK Signaling and Enable Persistence of Drug-Adapted BRAF-Mutant Melanoma Cells

Luca Gerosa,[1] Christopher Chidley,[1] Fabian Fröhlich,[1] Gabriela Sanchez,[1] Sang Kyun Lim,[1] Jeremy Muhlich,[1] Jia-Yun Chen,[1] Sreeram Vallabhaneni,[1] Gregory J. Baker,[1] Denis Schapiro,[1,2] Mariya I. Atanasova,[1] Lily A. Chylek,[1] Tujin Shi,[3] Lian Yi,[3] Carrie D. Nicora,[3] Allison Claas,[4] Thomas S.C. Ng,[5] Rainer H. Kohler,[5] Douglas A. Lauffenburger,[4] Ralph Weissleder,[5] Miles A. Miller,[5] Wei-Jun Qian,[3] H. Steven Wiley,[6] and Peter K. Sorger[1,7,*]

[1]Laboratory of Systems Pharmacology, Department of Systems Biology, Harvard Medical School, Boston, MA 02115, USA
[2]Broad Institute of MIT and Harvard, Cambridge, MA 02142, USA
[3]Biological Sciences Division, Pacific Northwest National Laboratory, Richland, WA 99354, USA
[4]Department of Biological Engineering, Massachusetts Institute of Technology, Cambridge, MA 02142, USA
[5]Center for Systems Biology, Massachusetts General Hospital Research Institute, Boston, MA 02114, USA
[6]Environmental Molecular Sciences Laboratory, Pacific Northwest National Laboratory, Richland, WA 99354, USA
[7]Lead Contact
*Correspondence: peter_sorger@hms.harvard.edu
https://doi.org/10.1016/j.cels.2020.10.002

SUMMARY

Targeted inhibition of oncogenic pathways can be highly effective in halting the rapid growth of tumors but often leads to the emergence of slowly dividing persister cells, which constitute a reservoir for the selection of drug-resistant clones. In $BRAF^{V600E}$ melanomas, RAF and MEK inhibitors efficiently block oncogenic signaling, but persister cells emerge. Here, we show that persister cells escape drug-induced cell-cycle arrest via brief, sporadic ERK pulses generated by transmembrane receptors and growth factors operating in an autocrine/paracrine manner. Quantitative proteomics and computational modeling show that ERK pulsing is enabled by rewiring of mitogen-activated protein kinase (MAPK) signaling: from an oncogenic $BRAF^{V600E}$ monomer-driven configuration that is drug sensitive to a receptor-driven configuration that involves Ras-GTP and RAF dimers and is highly resistant to RAF and MEK inhibitors. Altogether, this work shows that pulsatile MAPK activation by factors in the microenvironment generates a persistent population of melanoma cells that rewires MAPK signaling to sustain non-genetic drug resistance.

INTRODUCTION

Mutated BRAF (canonically $BRAF^{V600E}$) is found in ~50% of melanomas and results in constitutive activation of the mitogen-activated protein kinase (MAPK) signaling cascade, which comprises the RAF, MEK, and ERK kinases and thereby promotes proliferation. Oncogenic signaling by $BRAF^{V600E}$ can be blocked by FDA-approved inhibitors of RAF such as vemurafenib and dabrafenib or of MEK such as cobimetinib and trametinib. In patients, therapeutic responses to combined RAF and MEK inhibition therapy are often rapid and dramatic, but in most cases they are also transitory due to the emergence of drug-resistant clones (Groenendijk and Bernards, 2014). Emerging evidence suggests that rapid adaptation to targeted drugs by non-genetic mechanisms promotes sustained survival of persister cells, contributes to residual disease, and facilitates emergence of resistance mutations responsible for disease recurrence in patients (Pazarentzos and Bivona, 2015; Russo et al., 2019; Cipponi et al., 2020). However, the molecular mechanisms underlying drug adaptation, the emergence of persister cells, and selection for drug-resistant clones are only partially understood.

In melanoma cell lines, drug adaptation is observed soon after exposure to RAF/MEK inhibitors and gives rise to slowly dividing persister cells; this state is reversible following a drug holiday (Ramirez et al., 2016; Fallahi-Sichani et al., 2017; Shaffer et al., 2017; Paudel et al., 2018). Studies across a variety of cancer cell types and targeted therapies suggest that adaptive resistance is driven in part by signaling plasticity and changes in the activities of feedback mechanisms normally involved in regulating signaling cascades and receptor tyrosine kinases (RTKs) (Carver et al., 2011; Niederst and Engelman, 2013; Goel et al., 2016). The role of negative feedback is particularly well established in the case of $BRAF^{V600E}$ cancers: when $BRAF^{V600E}$ signaling is inhibited by drugs, synthesis of dual activity serine-threonine phosphatases (DUSPs) and other negative regulators of the MAPK cascade falls. This makes cells more sensitive to MAPK reactivation, for example, by growth factors in the tumor

CellPress
OPEN ACCESS

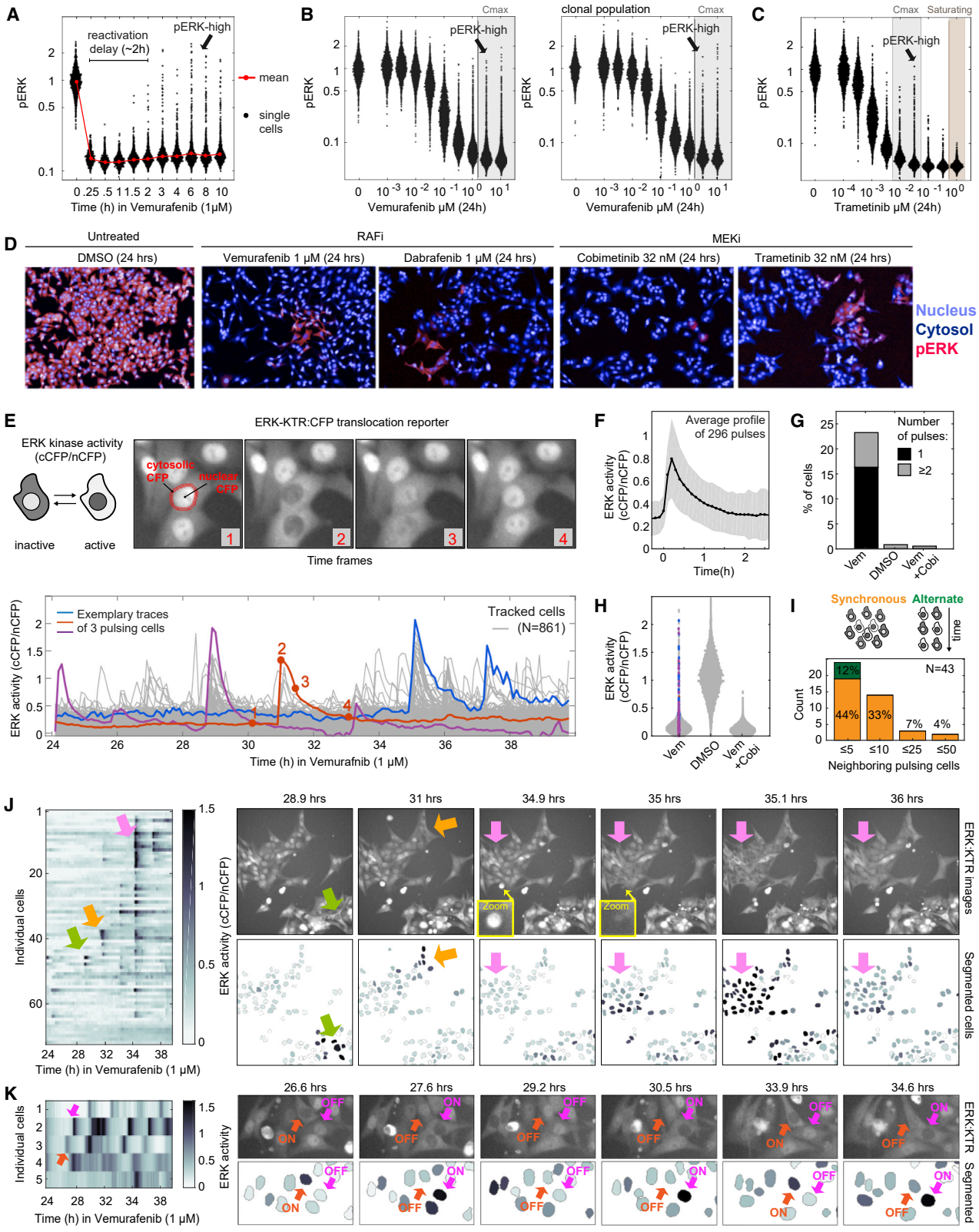

Figure 1. BRAF^{V600E} Melanoma Cells Exposed to RAF and MEK Inhibitors Exhibit Spatially Localized Pulsatile ERK Reactivation

(A) pERK levels by immunofluorescence microscopy in A375 cells treated with 1-μM vemurafenib.

(B) Single-cell pERK levels in parental (left) and clonal (right) A375 cells treated with vemurafenib for 24 h.

(legend continued on next page)

microenvironment (Lito et al., 2012; Chandarlapaty, 2012; Prahallad et al., 2012).

Despite elegant studies by Rosen and others (Lito et al., 2012; Sun et al., 2014), the mechanisms of adaptive MAPK reactivation in drug-treated $BRAF^{V600E}$ melanoma cells remain unclear. Some reports suggest that ERK remains largely inhibited (Pratilas et al., 2009; Montero-Conde et al., 2013; Fallahi-Sichani et al., 2015), whereas others suggest that it rebounds (Lito et al., 2012). Components of the extracellular environment, including growth factors involved in autocrine/paracrine signaling, have also been shown to promote resistance (Straussman et al., 2012; Wilson et al., 2012), but how mitogenic signals are transduced is unknown: similar to many other types of mammalian cells, melanocytes require MAPK activity to divide. Thus, a fundamental mystery of the persister state is how $BRAF^{V600E}$ melanomas can survive and proliferate when RAF and MEK inhibitors profoundly block MAPK signaling.

Here, we study the drug-adapted state of $BRAF^{V600E}$ melanoma cells using live- and fixed-cell imaging combined with proteomics and mathematical modeling. We find that drug-induced rewiring of the MAPK cascade causes $BRAF^{V600E}$ cells to experience sporadic ERK pulses of sufficient duration (~60–90 min) to promote cell survival and division. ERK pulses are triggered locally by factors in the microenvironment, likely released by neighboring cells. Thus, ERK is profoundly inhibited on average but briefly active in patches of cells, explaining the infrequent division characteristic of the drug-adapted state. A computational model shows that drug exposure mediates a shift between two configurations of the MAPK signaling cascade: from one driven by $BRAF^{V600E}$ that is drug sensitive to a second driven by receptors, Ras-GTP, and RAF dimers that is highly resistant to both RAF and MEK inhibitors. Moreover, accumulation of DNA damage and upregulation of error-prone polymerases (Russo et al., 2019) suggests a mechanism by which persister cells can acquire resistant mutations.

RESULTS

ERK Is Reactivated in a Subset of $BRAF^{V600E}$ Melanoma Cells Treated with RAF and MEK Inhibitors

Consistent with previous data (Lito et al., 2012), treatment of $BRAF^{V600E}$ A375 melanoma cells with vemurafenib at clinically relevant concentrations (1 μM) strongly suppressed the average activity of the MAPK cascade within 20 min, followed by a small rebound to ~5% of its initial level over the following 10 h (Figure 1A). When pERK levels were quantified in single cells by immunofluorescence imaging using antibodies against activating sites on $ERK1^{T202,Y204}$ and $ERK2^{T185,Y187}$ (hereafter pERK) (Figure 1A) we observed the rapid emergence (by t = 2 h) of a long-tailed distribution of pERK levels with 1%–5% of cells having pERK levels similar to those of drug-naive A375 cells. A similar phenomenon was observed in five A375 cultures that had been subjected to single-cell cloning (Figures 1B and S1A). Thus, pERK-high cells are unlikely to represent rare drug-resistant mutants. The same phenomenon was observed when cultures were treated with MEK inhibitors at clinically relevant concentrations (~10 nM; Figure 1C). However, at saturating drug concentrations (100-fold higher; ≥ 1 μM trametinib) pERK-high cells were absent, demonstrating a requirement for MEK activity (we explain below why MEK inhibitors inhibit signaling in all cells only at very high doses). When A375 cells were imaged following treatment with any of four RAF or MEK inhibitors at clinically relevant concentrations, high pERK staining was observed to occur in patches of neighboring cells (Figure 1D). Thus, the previously described phenomenon of MAPK rebound in drug-adapted BRAF-mutant melanoma appears to be caused by pERK reactivation in rare cells found in clusters.

ERK Pulses Spontaneously Arise in Neighboring Drug-Adapted $BRAF^{V600E}$ Melanoma Cells

To study ERK dynamics in single A375 cells, we transfected them with the fluorescence ERK-KTR:CFP activity reporter (Regot et al., 2014; Fallahi-Sichani et al., 2017) as well as geminin:RFP to score cell-cycle stage and H2B:YFP to facilitate tracking. The ERK-KTR:CFP reporter translocates from the nucleus to the cytosol when phosphorylated by ERK, providing time-resolved, single-cell data on kinase activity (Figure 1E, upper left panel). When reporter-expressing cells were exposed to 1-μM vemurafenib for 24 h and imaged every 6 min over a period of 16 h (N = 861 cells), ERK activity was profoundly inhibited, in agreement with fixed-cell data. However, cells sporadically underwent brief bursts of ERK reactivation at irregular intervals (see exemplary trajectories; Figure 1E, bottom panel). ERK pulses had a characteristic amplitude and duration: drug-inhibited ERK activity rose rapidly to a maximum level similar to that of untreated cells and then fell gradually to baseline within 60–90 min (Figure 1F). Over a 16-h period ~16% of cells (n = 134) exhibited a single ERK pulse and ~7% (n = 57) exhibited multiple pulses (Figure 1G). Thus, while fixed-cell imaging shows that only a small fraction of drug-treated A375 cells are pERK high at a specific point in time, live-cell imaging shows that this is true because of brief but frequent ERK pulses throughout the population (Figure 1H).

(C) Single-cell pERK levels in A375 cells treated with trametinib for 24 h.
(D) pERK staining in A375 cells treated with RAF and MEK inhibitors.
(E) ERK activity traces (N = 861) quantified by the ERK-KTR reporter from A375 cells treated with vemurafenib (1 μM, 24 h). Red numbers correspond to images in (E).
(F) Shape of average ERK pulse from 296 live-cell trajectories (solid line indicates mean and shading one standard deviation).
(G) Percentage of A375 cells with ERK pulses over a 16-h period.
(H) Single-cell ERK activity distributions of A375 treated with DMSO, vemurafenib (1 μM) alone, or with cobimetinib (1 μM). Colored dots denote ERK activity levels in the colored traces in (E).
(I) Percentage of ERK pulsing events that are synchronous or alternate in neighboring cells.
(J) Heatmap of ERK activity in cells treated with vemurafenib (1 μM, 24 h). Arrows denote ERK pulses; images of these pulses are shown on the right for the ERK:KTR CFP channel (upper row) and corresponding ERK activity (cCFP/nCFP ratio) (lower panel). Lysis of a dead cell preceding a synchronous ERK pulse event is shown in the magnified insert.
(K) Heatmap and image snapshots of ERK activity for neighboring cells exhibiting alternate ERK pulsing, shown as in (J).

CellPress
OPEN ACCESS

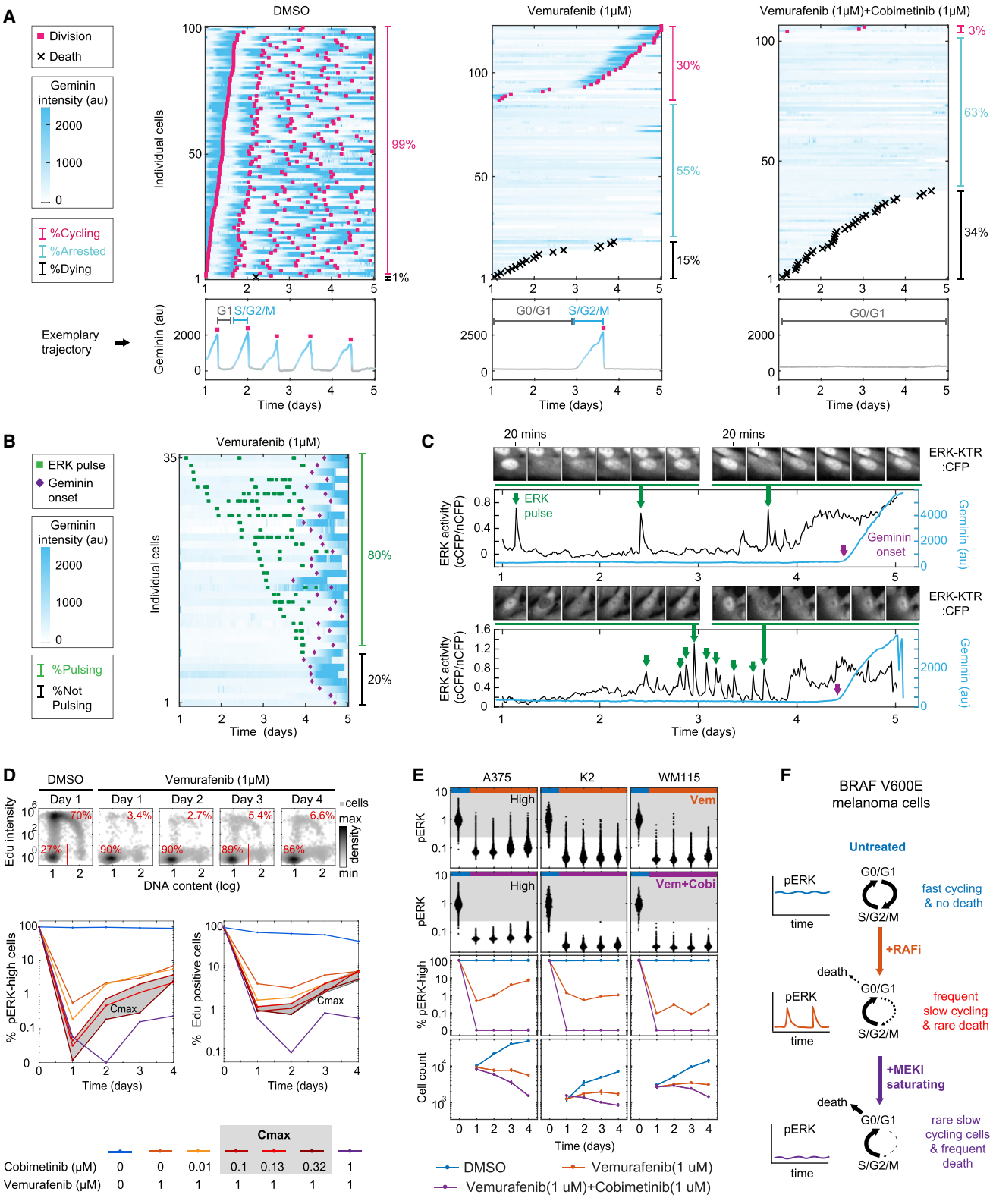

Figure 2. ERK Pulses Enable Slow Proliferation of Drug-Adapted BRAF^{V600E} Melanoma Cells

(A) Heatmap of geminin:RFP intensity for individual cells treated with DMSO, vemurafenib (1 μM) alone, or in combination with a saturating dose of cobimetinib (1 μM) for 24 h and then imaged for 4 days.

(B) Heatmap of geminin:RFP intensity for individual cells that escaped G0/G1 cell-cycle arrest after 4 days of vemurafenib (1 μM) treatment.

(legend continued on next page)

Live-cell movies also showed that neighboring cells often experienced a synchronous ERK pulse (88% of pulses, N = 43; Figure 1I). In other cases (12%), ERK pulsed in an alternating manner between neighboring cells, a behavior suggestive of a sender-receiver relationship (Figure 1K). Most ERK pulses involved five or fewer neighboring cells (44%), but some clusters involved more than 25 cells (11%) (Figure 1I). Nearby lysis of a dying cell was commonly observed in conjunction with a pulse (32%), as was contact of a dead cell body with a living cell (23%). In these cases, we often observed a wave of ERK activity (see images with magnified view, yellow boxes in Figure 1J). Within the largest pulses, which could involve up to 80 cells, ERK activity appeared to propagate over successive movie frames from a point of origin toward distant cells, taking up to ~20 min to reach to the furthest cells (Figure 1J; Video S1). Not all cells in such a wave of ERK pulses were in physical contact, suggesting a role for factors that diffuse into the media (see Figure 1J). We conclude that pulsatile reactivation of ERK occurs spontaneously in drug-adapted A375 cells and that spatiotemporal patterns are consistent with the autocrine-paracrine signaling previously implicated in regeneration of skin and other tissues (Hiratsuka et al., 2015).

ERK Pulses Enable Survival and Escape from Cell-Cycle Arrest of Drug-Adapted BRAF^{V600E} Melanoma Cells

To study the role of ERK pulses in cell survival and proliferation, reporter-expressing A375 cells were exposed to 1-μM vemurafenib and then imaged every 20 min for 4 days, starting 1 day after drug addition. Net cell number was constant over this period of time (Paudel et al., 2018), but data from >100 tracked cells revealed diverse outcomes at the single-cell level (Figure 2A). After 24-h drug treatment, geminin levels were low in most cells as a result of G0/G1 arrest, but over a 4-day period ~15% of cells died and ~30% divided once. Cells that managed to enter S phase progressed to mitosis only slightly more slowly (16 h) than untreated cells (12 h; Figure 2A) confirming that MAPK suppression primarily caused G0/G1 arrest. Among cells that divided in the presence of 1-μM vemurafenib (N = 35), 80% were observed to experience at least one ERK pulse (average 3.2 pulses; Figure 2B); in some cells as many as 9 pulses were observed prior to a division (Figure 2C; Videos S2 and S3). Among cells exposed to 1-μM vemurafenib plus a saturating concentration of cobimetinib (1 μM), ERK pulsing was fully suppressed and 35% of cells died; only 3% divided (Figure 2A). We conclude that pulsatile ERK activity is associated with slow proliferation and survival under drug treatment but that not every pulse results in cell division: as shown previously, the relationship between ERK pulsing and cell division is probabilistic (Albeck et al., 2013).

When A375 cells were exposed to vemurafenib (1 μM) and cobimetinib for 1 to 4 days over a 100-fold concentration range (0.01–1 μM) and assayed by fixed-cell microscopy, the fraction of pERK-high cells fell 10 to 1,000-fold compared with DMSO-treated cells. Over a range of cobimetinib doses and times of exposure, the reduction in the number of S-phase cells (monitored using EdU pulse-labeling) closely paralleled the reduction in pERK-high cells (Figure 2D). Similar results were obtained in seven other BRAF-mutant melanoma lines. In the presence of 1-μM vemurafenib, depending on the line, 0.1% to 10% of cells were pERK high, cell number remained roughly constant over a 4-day period, and the addition of cobimetinib eliminated pERK-high cells and caused net cell loss (Figures 2E and S1B). These data suggest that in multiple cell lines representing a range of sensitivities to RAF inhibitors, cells escaping cell-cycle arrest experience ERK pulses; conversely, inhibiting ERK pulsing suppresses cell division and increases cell death to a similar degree (Figure 2F).

Multiple Receptors Promote ERK Pulsing in Drug-Adapted BRAF^{V600E} Melanoma Cells

The spatiotemporal pattern of ERK pulses in live-cell movies is suggestive of paracrine/autocrine signaling mediated by transmembrane receptors. To investigate the role of RTKs in generating spontaneous ERK pulses, we treated vemurafenib-adapted A375 cells (1 μM, 36 h) with inhibitors of the EGFR/ERBB receptors (lapatinib or poziotinib), FGFR (infingratinib), or AXL (R428) at 1 μM; alternatively cells were treated with a SHP2 phosphatase inhibitor (SHP099, 5 μM) or pan-RAF inhibitor (LY3009120 at 1 μM) for 2 h. Pan-RAF inhibitors are active against BRAF/CRAF homo- and heterodimers downstream of active RTKs, whereas vemurafenib and dabrafenib inhibit only BRAF^{V600E} monomers. In this experiment, a saturating concentration of cobimetinib served as a positive control for full inhibition of pulsing (Figure 3A). We found that inhibition of RTKs and of SHP2 partially blocked pulsing, as evidenced by a change in the distribution of pERK-high cells. Combinations of drugs were generally more active than single agents. Pan-RAF inhibitors inhibited pulsing over multiple days of drug exposure whereas SHP099 acted transiently (Figure 3B), but neither was as effective as 1-μM cobimetinib (Figures 3A and S1C). We conclude that ERK pulsing is mediated by RAF dimers, MEK and, to a lesser extent, by SHP2 and that these lie downstream of multiple RTKs (Figure 3C).

Quantitative ELISA and immunofluorescence imaging showed that ERBB, cMet, and AXL receptors were present on vemurafenib-adapted A375 cells (1 μM, 24 h) at 10^2–10^4 copies per cell, a low level as compared with abundances in colorectal or breast cancer cells (Figure 3D). To show directly that these receptors activate immediate-early signal transduction in adapted cells, A375 cells were treated with vemurafenib (1 μM, 24 h) and then with growth factors EGF, NRG1, FGF8, or HGF (100 ng/mL). Phosphorylation of downstream signaling proteins was monitored by immunofluorescence. We observed that all cells in the population underwent rapid and transient phosphorylation of a kinase cascade comprising pMEK, pERK, p90RSK^{T359}, pS6$^{S240/244}$, and pS6$^{S235/236}$ (Figures 3E, S2A and S2B). RNA-seq of these cells showed that ~80 genes were upregulated 3-

(C) ERK activity and geminin:RFP intensity for two exemplary cells from (B).
(D) Percentage of pERK-high cells and EdU positive A375 cells treated with vemurafenib (1 μM) and varying cobimetinib concentrations for 4 days.
(E) Single-cell pERK distributions for three BRAF^{V600E} melanoma cell lines treated with 1-μM vemurafenib alone (1st row) or in combination with 1-μM cobimetinib (2nd row) and percentage of pERK-high cells (3rd row) and cell counts (4th row) during treatment.
(F) Schematic depiction of relationship between ERK pulsing and slow cycling in drug-adapted BRAF-mutant melanoma cells.

CellPress
OPEN ACCESS

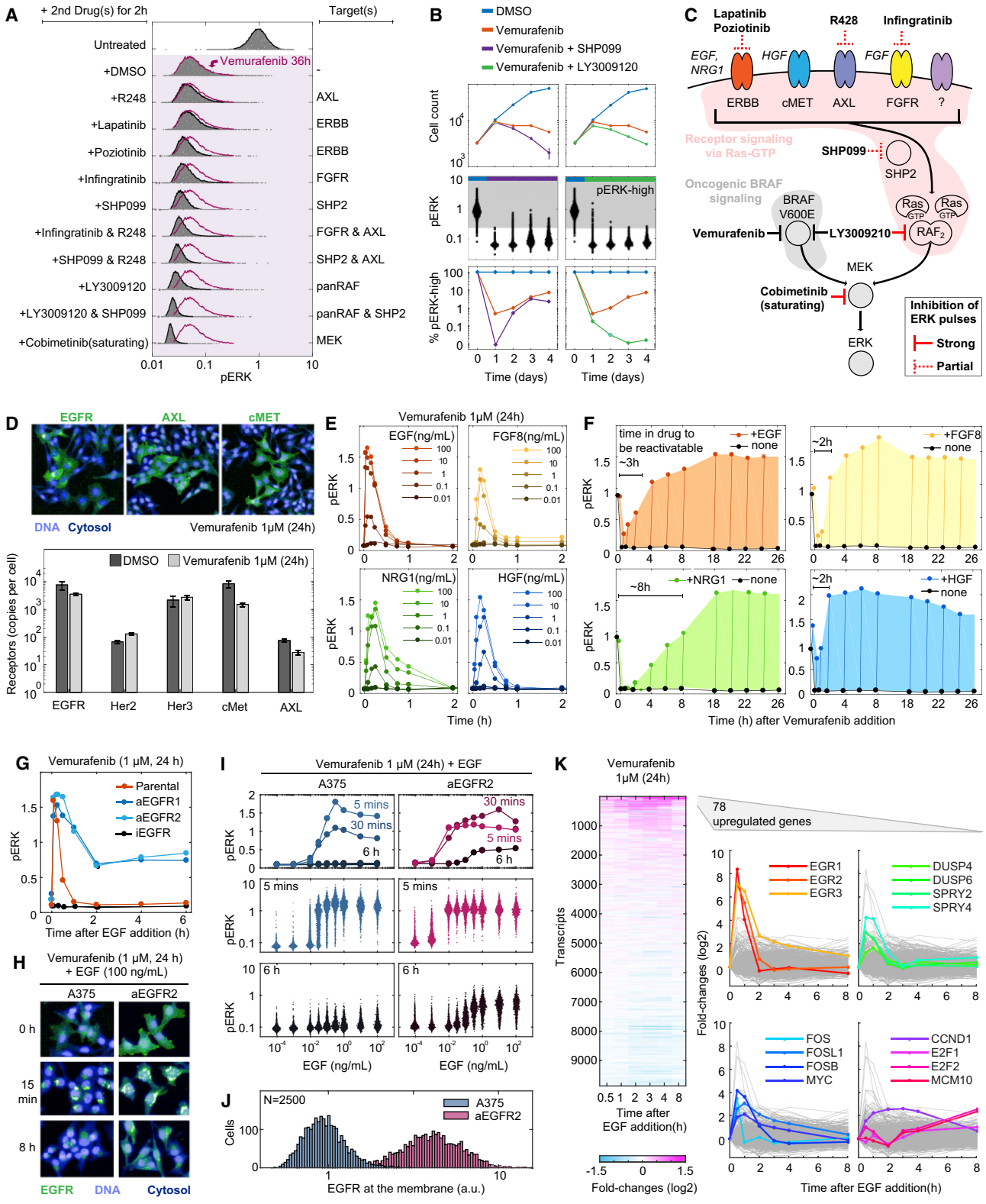

Figure 3. Drug-Adapted BRAF^{V600E} Melanoma Cells Can Use Multiple Receptors to Induce ERK Pulses

(A) pERK distributions of A375 cells treated for 36 h with vemurafenib followed by addition of inhibitory drugs for 2 h.

(B) Cell count (1st panel), single-cell pERK distribution (2nd panel), and percentage of pERK-high cells (3rd panel) for A375 cells treated for 4 days with single or combinations of MAPK cascade targeted inhibitors.

(legend continued on next page)

fold or more including immediate-early response genes, such as EGR1 and FOSL1, and feedback regulators, such as DUSP4/6 and SPRY2/4 (Figures 3K and S2C). Immediate-early genes peaked 1–2 h after ligand addition and genes promoting G1 to S transition, such as CCND1 (cyclin D) and E2F1/2, peaked between 2 and 8 h. From these data we conclude that despite the low abundance of RTKs, exposure of drug-adapted cells to one of several different growth factors induces a synchronous ERK pulse across a population of cells as well as transient expression of mitogenic genes; the amplitude and dynamics of this ERK pulse resemble spontaneous pulses in single cells.

Low Receptor Abundances Limit the Duration of ERK Pulses and Diversify Responsiveness to Ligand

Based on current understanding of receptor signaling, we hypothesized that the expression of RTKs at low levels in melanoma cell lines served to limit the duration of ligand-induced ERK reactivation (Resat et al., 2003). Consistent with this, EGF was internalized into endosomes in A375 cells within 15 min of EGF addition and overall receptor levels fell 3-fold within 24 h (Figure S2D). When CRISPRa was used to overexpress EGFR by ~5–8-fold (Figure S2E and S2F), the addition of EGF to vemurafenib-adapted cells (1 μM, 24 h) caused sustained rather than transient ERK activation (Figure 3G). Moreover, a substantial fraction of receptor remained at the plasma membrane following ligand addition (Figure 3H) and cells were ~100-fold more sensitive to EGF than parental cells, with ERK activation observed at concentration of EGF as low as 0.01 ng/mL (1 pM; Figure 3I). Imaging showed that at low EGF doses, pERK was activated in all EGFR-overexpressing cells but only a subset of parental cells. Thus, differences in EGFR expression levels, whether engineered by CRISPRa or naturally occurring (receptor levels are log-normally distributed in parental cells; Figure 3J) can alter the sensitivity of cells to growth factors. Receptors levels are often correlated among neighboring cells (Shaffer et al., 2017) (Figure 3D), and this may explain why pulsing occurs in patches. Low receptor levels, and efficient internalization from the cell surface, likely explain why pulses are transient.

Proteomics Reveals Relief of Negative Feedback on Receptor Signaling in Drug-Adapted Melanoma Cells

To quantify the effects of MAPK inhibition on feedback regulators, we performed quantitative targeted mass spectrometry and RNA-seq on A375 cells treated for 24 h with four doses of vemurafenib (from 0.01 to 1 μM). This allowed us to determine the absolute abundances, phosphorylation states, and transcript levels of 21 proteins or genes in the MAPK pathway at different levels of ERK inhibition (Figures 4A–4D; see Table S1). In untreated A375 cells ~20%–30% of total ERK1 and ERK2 was phosphorylated on T202/Y204 and T185/Y187; this fell to 2%– 3% phosphorylation in cells treated with 1-μM vemurafenib (Figure 4D). The abundances of six proteins, including the EGF receptor, SPRY2/4, the ERBB inhibitor MIG6, and DUSP4/6 fell by 2.5- to 35-fold with vemurafenib exposure; other protein levels were unchanged (Figure 4B). RNA-seq data showed that genes for these six proteins were also downregulated at the transcript level (Pratilas et al., 2009) (Figure 4C). Analyzing stoichiometric ratios of interacting proteins provided additional insight into feedback regulation (Figure S3A). For example, when MAPK signaling was fully active (in the absence of vemurafenib) SPRY2 and SPRY4 were in 6-fold stoichiometric excess to GRB2, but in cells exposed to 1-μM vemurafenib for 24 h, GRB2 was in 5-fold excess to SPRY2/4 (Figures 4B and S3A). SPRY2 competitively inhibits recruitment of the RAS guanine nucleotide exchange factor SOS1 to GRB2 (Lao et al., 2006), and observed protein levels in A375 cells are therefore precisely in the range needed to modulate RTK signaling via RAS. A substantial change in stoichiometry (from ~1:10 to 1:100) was also observed for the DUSP4/6 phosphatases relative to their ERK1/2 targets (Figures 4B and S3A). Finally, the phosphorylation of SOS1 on S1134, which reduces SOS1 activity and SOS1-GRB2 association (Saha et al., 2012), fell from 100% to 20% of total protein following vemurafenib exposure (Figure 4D). These data show that multiple proteins involved in negative regulation of receptor and MAPK signaling fall in direct proportion to the degree of MAPK inhibition (Lito et al., 2012). However, even when ERK is largely inhibited (at 1-μM vemurafenib), phosphorylation of EGFR, CBL, GRB2, and SHP2 remains low (<5% of total protein) (Figure 4D). Thus, drug-induced relief of negative feedback prepares melanoma cells for RTK activation but is insufficient for strong ERK activation in absence of exogenous growth factors.

Receptor-Mediated Signaling in Drug-Adapted Cells Is Resistant to RAF and MEK Inhibitors

To quantify the effects of growth factors on drug-adapted cells, we pre-treated them for 24 h with RAF inhibitors across a 10^4-fold concentration range, added various growth factors and then measured pERK and pMEK levels by immunofluorescence 5 min later (the peak of the synchronized pulse in the cell population). We found that the inducibility of pERK and pMEK (red and orange lines, Figure 4E) correlated directly with the degree of

(C) Schematic of reduction in spontaneous ERK pulses achieved by co-targeting MAPK cascade components in addition to vemurafenib.
(D) Receptor abundance by immunofluorescence (top) and ELISA (bottom) in A375 cells with and without vemurafenib treatment for 24 h.
(E) pERK in cells exposed to different concentrations of growth factors in A375 cells exposed to vemurafenib for 24 h.
(F) pERK levels in cells exposed to growth factors (100 ng/mL) for 15 min at different times after the addition of vemurafenib. Shading interpolates maximal pERK levels.
(G) pERK levels for parental, CRISPRa EGFR overexpressing (aEGFR1 and aEGFR2), and CRISPRi EGFR downregulated cell lines and exposed to vemurafenib for 24 h and then to EGF (100 ng/mL).
(H) EGFR localization by immunofluorescence microscopy in normal and EGFR-overexpressing cells exposed to vemurafenib for 24 h and then to EGF (100 ng/mL).
(I) Population-level and single-cell pERK levels in A375 and A375 EGFR-overexpressing (aEGFR2) cells exposed to vemurafenib (1 μM, 24 h) and then to 5 min of EGF over a 10^6-fold concentration range.
(J) EGFR abundance by immunofluorescence microscopy at the membrane of A375 or A375 EGFR-overexpressing (aEGFR2) cells exposed for 24 h to 1-μM vemurafenib.
(K) Transcript levels in A375 cells exposed to vemurafenib for 24 h and then EGF (100 ng/mL).

CellPress
OPEN ACCESS

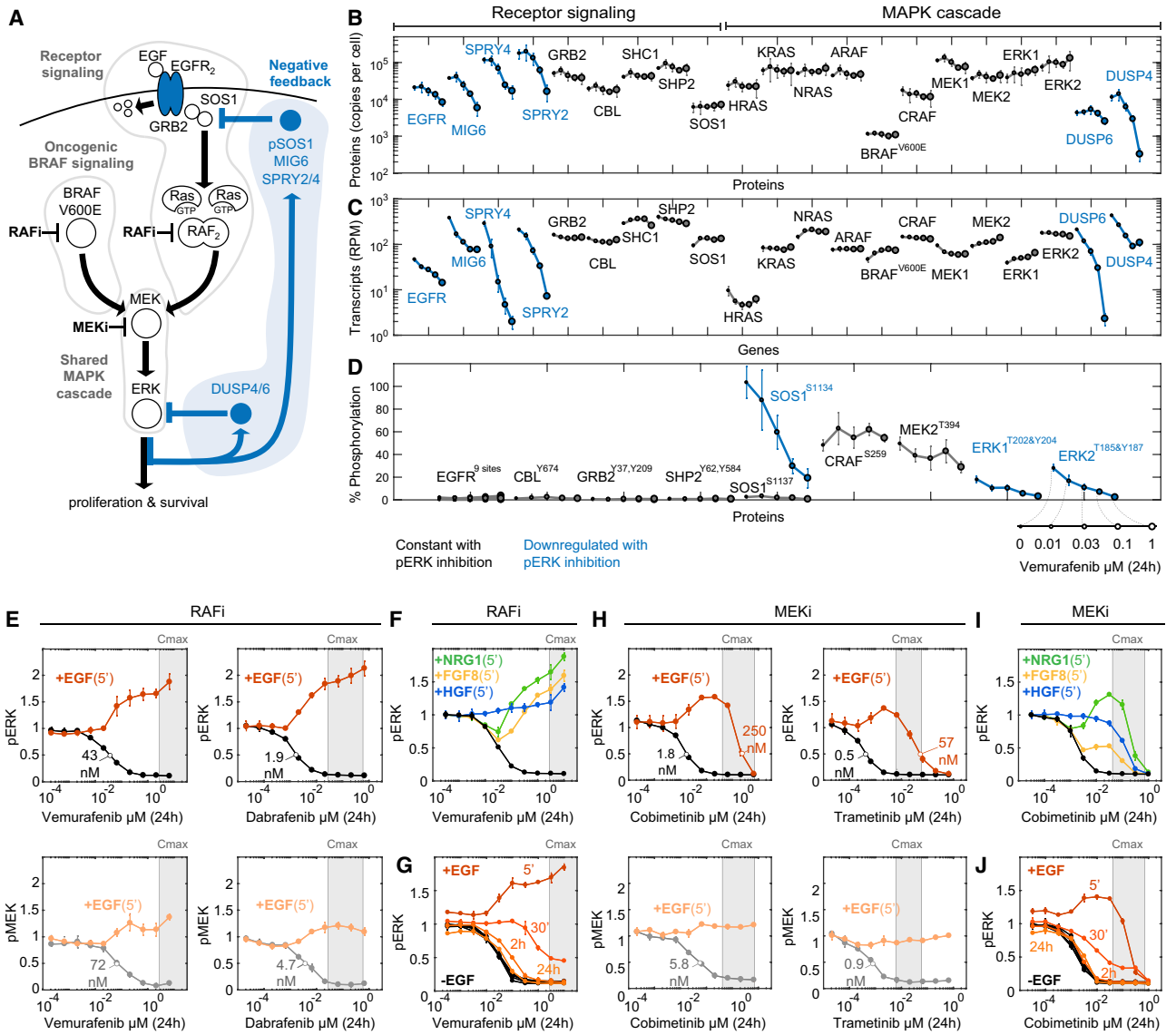

Figure 4. Quantitation and Effects of Negative Feedback Relief and Receptor Activation on MAPK Signaling in Melanoma Cells Exposed to RAF and MEK Inhibitors

(A) Schematic of the ERK pathway in BRAF^{V600E} cells; negative feedback regulators are shown in blue.

(B) Absolute abundances of MAPK pathway proteins by proteomics following 24-h exposure to vemurafenib at the doses indicated in D.

(C) Changes in mRNA levels by RNA-seq for the same proteins.

(D) Phosphorylation of key regulatory sites on selected proteins by phosphoproteomics.

(E–G) pERK and pMEK levels following 24-h exposure of cells to vemurafenib or dabrafenib followed by addition of EGF (100 ng/mL) for 5 min (E), of NRG1, FGF8, and HGF (100 ng/mL) for 5 min (F), or EGF (100 ng/mL) for indicated amount of time (G).

(H–J) pERK and pMEK levels following 24-h exposure of cells to cobimetinib or trametinib followed by addition of EGF (100 ng/mL) for 5 mins (H), or NRG1, FGF8, or HGF (100 ng/mL) for 5 min (I), or EGF (100 ng/mL) for the times indicated (J).

(B–D), error bars indicate standard deviations from four replicates.

(E–J), error bars indicate standard deviations from two replicates.

pre-treatment ERK inhibition (black lines, Figure 4E). ERK was transiently activated to a level above its resting (BRAF^{V600E}-driven) level in drug-naive A375 cells by all four growth factors tested (Figures 4F and 4G).

Since MEK kinases lie downstream of both oncogenic BRAF^{V600E} and receptor-mediated RAF signaling, MEK inhibitors should, in principle, block both receptor-driven and BRAF^{V600E}-driven signaling with similar efficacy. However, in cells incubated with MEK inhibitors for 24 h and exposed to EGF for 5 min, a 100-fold higher drug concentration was needed to inhibit pERK (IC_{50} ~250 nM for cobimetinib and 50 nM for trametinib) than in the absence of ligand stimulation (IC_{50} ~2 nM and 0.5 nM respectively). Moreover, across a 10^4 range of MEK inhibitor concentrations, EGF-induced pERK levels rose

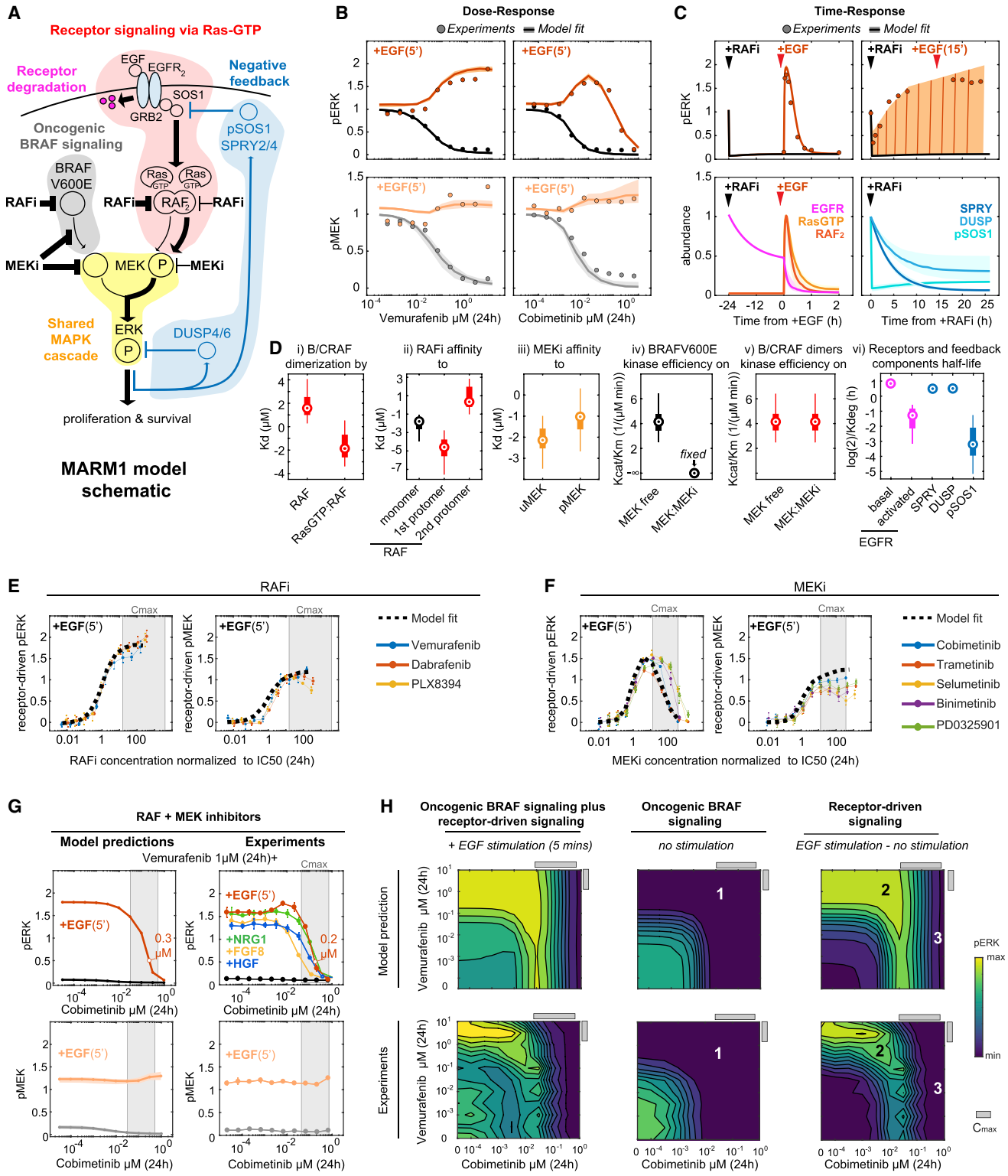

Figure 5. Computational Modeling of ERK Pulsing during Combined RAF and MEK Inhibition

(A) Species and interactions in the MARM1 computational model.

(B) Model simulations of protein species (solid lines indicate median values and shades interquartile ranges) and their fits to experimental data (dots). pERK (upper panels) and pMEK (low panels) levels after exposure of cells to EGF for 5 min in the presence of varying concentrations of vemurafenib or cobimetinib for 24 h.

(C) Model simulations of pERK levels and protein abundances in cells treated with vemurafenib for 24 h. t = 0 represents the time of EGF addition in the left panel and of vemurafenib in the right panel.

(legend continued on next page)

to a level above those in drug-naive cells and then fell to background levels, giving rise to a biphasic dose-response curve. Full suppression of pERK was observed only at MEK inhibitor doses >100-fold above clinically relevant concentrations (~1 μM; Figure 4H). A similar biphasic response of pERK to cobimetinib was observed using three other growth factors (Figures 4I and 4J). Thus, RTK-mediated ERK activation is much more resistant to MEK inhibition than $BRAF^{V600E}$ oncogenic signaling.

We also observed that, in the absence of added ligands or vemurafenib pre-treatment, MEK inhibitors were potent in reducing pMEK levels (IC_{50} ~6 nM for cobimetinib and 0.9 nM for trametinib). This is surprising because protein kinase inhibitors usually act by blocking the ability of kinases to phosphorylate downstream substrates, in this case ERK, and not by blocking phosphorylation of the kinase being inhibited (i.e., MEK). We speculate that MEK inhibitors, which act allosterically and bind outside of the kinase active site, disrupt $BRAF^{V600E}$ interaction with MEK (Figure 4H). Strikingly, the same MEK inhibitors did not block MEK phosphorylation mediated by growth factors (Figure 4H). To better understand the mechanisms responsible for these and other data we turned to a mechanistic computational model that recapitulates key properties of the MAPK pathway.

Construction of a Computational Model of Oncogenic and Receptor-Driven MAPK Signaling in the Presence of RAF and MEK Inhibitors

To study mechanisms of ERK pulsing during RAF and MEK inhibition *in silico*, we constructed a mass-action biochemical model of MAPK signaling (melanoma adaptive resistance model; MARM1) using the rule-based PySB framework (Lopez et al., 2013) incorporating diverse structural, biochemical, pharmacological, and cell-level data. MARM1 extends previously published MAPK models (Kholodenko, 2015; Rauch et al., 2016; Rukhlenko et al., 2018) using an energy-based formulation that better describes cooperativity in protein-protein and protein-drug interactions (Lopez et al., 2013; Sekar et al., 2017) (see Data S1). The model includes (1) growth-factor-dependent activation of RTKs that are then internalized and degraded (Figures 3G and 3H), (2) negative feedback mediated by SOS1, SPRY2/4, and DUSP4/6 (as described above; Figure 4A), (3) formation of active hetero- and homo-CRAF/BRAF dimers by Ras-GTP binding, downstream of activated RTKs (Freeman et al., 2013), (4) lower affinity of RAF inhibitors for CRAF/BRAF dimers than $BRAF^{V600}$ monomers (Yao et al., 2015; Kholodenko, 2015; Rukhlenko et al., 2018), (5) efficient phosphorylation of MEK by RAF dimers but not by $BRAF^{V600E}$ when MEK is bound to an allosteric MEK inhibitor (Lito et al., 2014), and (6) a lower affinity of MEK inhibitors for phosphorylated versus unphosphorylated MEK (Hatzivassiliou et al., 2013). The resulting model has 11 protein components (shown in Figure 5A) and 1,007 ordinary differential equations with 70 kinetic parameters. Strikingly, the core MAPK cascade comprising just RAS, $BRAF^{V600E}$, CRAF, MEK, and ERK, bound and unbound to inhibitory drugs involved over 200 distinct protein complexes differing in biochemical activity and drug-binding properties, highlighting the need for a systematic analysis of the configurations in which MAPK signaling operates in melanoma cells. Initial conditions and kinetic rates were estimated from mass spectrometry data and time course or dose-response data on pMEK and pERK signaling in the presence of absence of RAF and MEK inhibitors (Figures 5B–D, S4A, and S4B). The model precisely recapitulated time- and dose-responses of BRAF-mutant melanoma cells treated with RAF or MEK inhibitors and EGF ligand (Figures 5B and 5C), demonstrating that molecular mechanisms included in the model were sufficient to explain the experimental data.

Computational Modeling Shows that RAF and MEK Complexes Assembled by Transient Receptor Signaling Are Less Inhibitable by Drugs than the Analog Complexes in the Oncogenic Configuration

Analysis of the model helped to elucidate the molecular mechanisms underpinning the ability of activated receptors to induce ERK signaling during RAF or MEK inhibition. The MARM1 model indicated the possible simultaneous existence of two relatively distinct MAPK configurations, an oncogenic configuration driven by monomeric $BRAF^{V600E}$ and a "physiological" configuration driven by RTKs and involving RAS-GTP and BRAF/CRAF dimers. Parameter estimation and simulations confirmed that whereas $BRAF^{V600E}$ monomers had a high affinity for vemurafenib and similar drugs, only one protomer in a B/CRAF dimer bound drug avidly making dimers drug resistant (Figure 5Dii). Oncogenic signaling promoted synthesis of negative regulators, such as DUSPs and SPRY proteins, but many of these act upstream of BRAF, making negative feedback more effective against the physiological than oncogenic configuration. When $BRAF^{V600E}$ was inhibited, negative regulation was relieved, placing the physiological configuration in a latent state that could be activated by ligand. Only when ligands were present did RTKs dimerize, recruit GRB2:SOS1 and generate RAS-GTP (Figure 5C). Binding of RAS-GTP to B/CRAF increased hetero-/homodimerization affinity by 10^4-fold (relative to the basal affinity of unbound RAFs; Figure 5Di). A concomitant fall in DUSP levels allowed for twice as much pERK than in the oncogenic signaling state, even at similar pMEK levels (Figure 5B), explaining the potentiation of ERK signaling by receptors. The estimated half-lives of SPRY and DUSP proteins also explained why ~2 h are required for negative feedback to decay and cells to become fully sensitive to growth

(D) Distributions of kinetic parameters from 100 estimation runs. Dot indicates median, thick bars interquartile ranges, and thin lines the minimum and maximum values in $\log_{10}$ scale. Note that the rate for $BRAF^{V600E}$ phosphorylation of MEK when MEK is bound by MEKi was set to zero.
(E and F) Calculated net receptor-driven ERK signaling as the difference between pERK levels in EGF stimulated cells (5 min) and unstimulated cells following pretreatment for 24 h with the indicated RAF (E) or MEK (F) inhibitors. Measurements (colored lines) are shown overlaid to model fits (dotted black line).
(G) Model predictions (left panels) and experimental validation (right) of pERK (upper rows) and pMEK (lower rows) in cells treated for 24 h with vemurafenib (1 μM) plus cobimetinib with or without subsequent addition of EGF, NRG1, FGF8, or HGF (100 ng/mL for 5 min). For simulations, solid lines indicate median values and shades interquartile ranges. For experiments, error bars indicate standard deviations from two replicates.
(H) Model simulation (top panels) and experimental validation (bottom panels) of pERK levels following 24-h exposure to vemurafenib plus cobimetinib in A375 cells exposed to EGF (100 ng/mL for 5 min) (left column), without addition of EGF (central column), and subtraction of the two to estimate net receptor-driven ERK activity (right column).

factors (Figures 5C and 5Dvi). A decrease in the half-life of RTKs in the plasma membrane from ~10 h to ~5 min upon activation by ligands explained rapid pulse termination by receptor internalization and degradation (Figures 5C and 5Dvi).

Additional experiments showed that when the physiological MAPK configuration was induced with EGF and one of three RAF inhibitors added, pERK and pMEK levels (which are driven by receptor signaling under these conditions) rose monotonically as a result of relief of negative feedback (Figure 5E). The calibrated model recapitulated this finding (the net contribution from activated receptors was estimated in this case by subtracting pMEK and pERK levels in unstimulated cells from the corresponding signals in EGF stimulated cells; see STAR Methods). When the data were normalized to drug affinity (as determined by IC_{50} values *in vitro*) the three RAF inhibitors behaved similarly (Figure 5E). When any one of five MEK inhibitors were used, the receptor-driven contribution to pERK levels exhibited a bell-shaped dose-response curve (Figures 5F, S3B, and S3C). Modeling showed that, at clinically relevant drug concentrations, MEK inhibitors were similar to RAF inhibitors in blocking oncogenic signaling, relieving negative feedback and allowing potent receptor-driven signaling. However, when growth factors were present, inhibition of physiological signaling required 100-fold more MEK inhibitor (Figure 5F). Two molecular mechanisms were responsible for this differential sensitivity to drug in the model: (1) inhibition of MEK phosphorylation by $BRAF^{V600E}$ occurred near the drug IC_{50}, but MEK phosphorylation by BRAF/CRAF dimers was not affected because RAF dimers can phosphorylate MEK even when it is bound by MEK inhibitors, presumably due to the different stereochemistry of the underlying complexes (Hatzivassiliou et al., 2013; Lito et al., 2014) (Figures 5Div and 5Dv); (2) once MEK is phosphorylated, its affinity for MEK inhibitors falls ~10-fold, resulting in less potent inhibition of ERK phosphorylation, as estimated by model parameters (Figure 5Diii). Thus, modeling shows that a large pool of pMEK is generated by growth-factor-bound RTKs via the physiological MAPK configuration, and this pool is fully drug-bound only when MEK inhibitors are used at ~1 μM; thus, it is only at these clinically inaccessible concentrations that ERK pulsing is fully blocked (Figures 5B and 5F). Modeling therefore provides a precise mechanistic explanation for the resistance of the receptor-driven physiological MAPK configuration, relative to the oncogenic configuration, to both RAF and MEK inhibitors.

RTK-Mediated ERK Pulsing Can Occur over a Wide Range of Combined RAF and MEK Inhibitor Concentrations

To test the predictive capabilities of the MARM1 model trained against single-agent dose-response data, we predicted the resistance of receptor-driven ERK signaling to combined RAF and MEK inhibition (Figure 5G). When we simulated the effects of adapting cells to different concentrations of cobimetinib plus 1-μM vemurafenib (for 24 h) and then exposing them to EGF for 5 min, we predicted that (1) pMEK levels would increase ~10-fold above baseline levels and be insensitive to inhibition by increasing cobimetinib concentrations and (2) the IC_{50} for pERK inhibition would be >100-fold higher than for oncogenic signaling (increasing from ~2 to 300 nM; Figure 5G). Experiments confirmed these predictions, which could be recapitulated with three growth factors other than EGF (Figure 5G) and with trametinib plus dabrafenib (Figure S3D). We conclude that MEK phosphorylation in the presence of any one of several different growth factors is a mechanism of resistance to MEK and RAF inhibitors in combination. We then used the model to simulate isobolograms for the oncogenic MAPK configuration, the receptor-driven configuration, and their joint total pERK control (Figures 5H and S4C). Experimental data were collected under the same conditions in the presence and absence of vemurafenib and EGF and corresponding isobolograms then computed (see STAR Methods for details). Both experiments and simulations showed that oncogenic signaling (which predominates at point "1" in the isobologram; Figure 5H) was inhibited by MEK and RAF inhibitors acting in a roughly additive manner at doses well below the clinically accessible ranges (gray bars). In contrast, RTK-driven MAPK signaling induced by ligand addition was highly resistant to RAF/MEK inhibitors used in combination (point "2"; Figure 5H) and only at the highest, clinically inaccessible doses did MEK inhibitors behave as single-agent antagonists of pERK (point "3"). Thus, RTK-mediated ERK reactivation—which experiments show is pulsatile—can occur over a wide range of combined RAF and MEK inhibitor concentrations.

ERK Pulses Can Be Observed *In Vivo* in Mouse Xenografts

To determine if ERK pulses occur in *in vivo*, A375 xenografts were grown in nude mice and both fixed- and live-cell imaging performed. For fixed-cell imaging mice were treated for 5 days with dabrafenib (25 mg/kg q.d.) plus trametinib (2.5 mg/kg q.d.), and tumors were recovered, formaldehyde fixed and paraffin embedded (FFPE), and subjected to immunofluorescence imaging (Lin et al., 2018). Single cells were identified by segmentation using nuclear staining; pERK was quantified in the nucleus and surrounding cytoplasm ($n > 10^4$ cells; 3–4 animals per condition, Figure S5A). We observed that pERK levels were substantially reduced in the great majority of tumor cells from animals treated with dabrafenib plus trametinib but that clusters of pERK-high cells were still present, and these were found in clusters similar in size to those found in drug-adapted cell cultures (Figures 6A and S5A–S5C).

To study ERK dynamics, we performed intravital imaging of A375 tumors expressing the ERK-KTR and geminin reporters. Movies of ~4 h in duration and having a sampling interval of ~6.5 min were recorded from three mice that had been exposed to dabrafenib plus trametinib (for 2 days) and also from control animals. Once again, ERK was largely inhibited under drug treatment but we observed multiple examples of pulsatile ERK reactivation in small clusters of cells (1–3 cells) (Figure 6B and Video S4 for two examples). Some cells also underwent division (Figure S5D). These findings are consistent with the idea that sporadic ERK pulses and slow cell proliferation occur in xenografted melanoma tumors in which oncogenic $BRAF^{V600E}$-driven ERK signal has been inhibited by a RAF plus a MEK inhibitor.

A Possible Connection between the Drug-Adapted Persister State and Replication Stress

It has recently been shown that treatment of $BRAF^{V600E}$ colorectal cancer cells with MAPK inhibitors induces a mutagenic state that

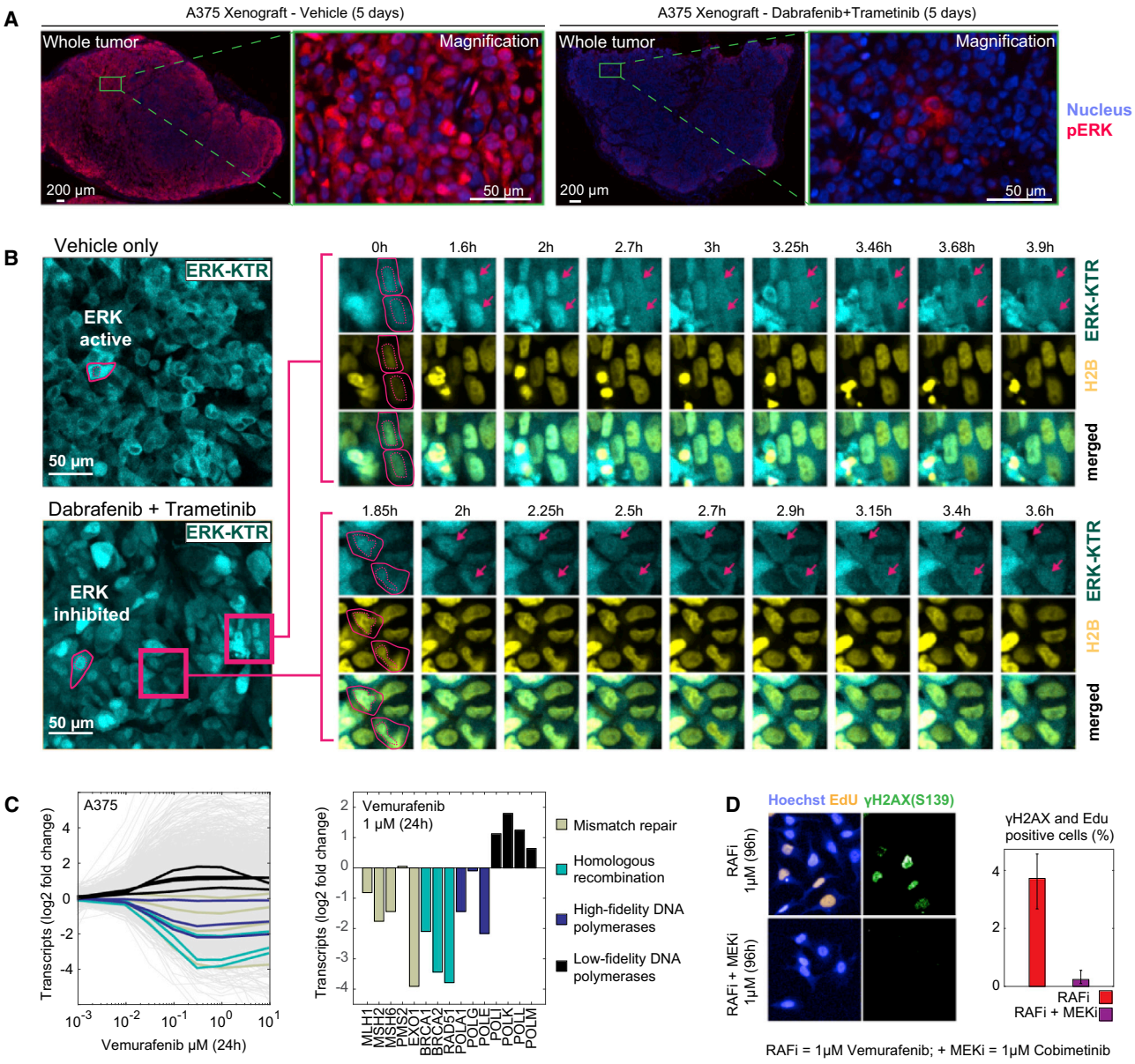

Figure 6. ERK Pulsing in Mouse Xenografts and Replication Stress in Drug-Adapted Melanoma Cells

(A) Immunofluorescence microscopy of pERK in A375 mouse xenografts treated either with vehicle alone or dabrafenib plus trametinib for 5 days.

(B) Intravital imaging of A375 fluorescent reporter cells in mouse xenografts treated for 48 h with vehicle alone or dabrafenib plus trametinib. For drug-naive tumors, a ERK-KTR:CFP field of view is shown; for tumors in drug-treated animals a field of view and two time courses are shown with ERK-KTR:CFP above and H2B:YFP below. Arrows indicate cells identified to undergo an ERK pulse.

(C) Expression of genes involved in DNA repair and of DNA polymerases in A375 cells treated for 24 h with vemurafenib at different doses (line plots, left) or with 1-µM vemurafenib (bar plots, right).

(D) EdU and p-γH2AX staining in A375 cells treated for 96 h with vemurafenib (1 µM) alone or in combination with saturating doses of cobimetinib (1 µM). Percentage of cells having incorporated EdU or positive for γH2AX staining is shown. Error bars indicate standard deviations from three replicates.

may facilitate acquisition of drug-resistance mutations (Russo et al., 2019). When we analyzed gene expression in A375 cells treated with vemurafenib for 24 h, we identified a gene expression signature similar to the one described by Russo et al. It includes the dose-dependent downregulation of genes involved in DNA repair and upregulation of error-prone DNA polymerases (Figure 6C). In drug-adapted cells (1-µM vemurafenib; 96 h) we observed that ~5% of cells were synthesizing DNA (as measured by EdU incorporation) and that most of these cells stained positive for diffuse γ-H2AX, a marker of replication stress (Figure 6D). Thus, slowly dividing drug-adapted melanoma cells appear to have the properties of the mutation-prone persister state—replication stress and upregulation of error-prone polymerases—previously observed in colorectal cancer cells (Russo et al., 2019).

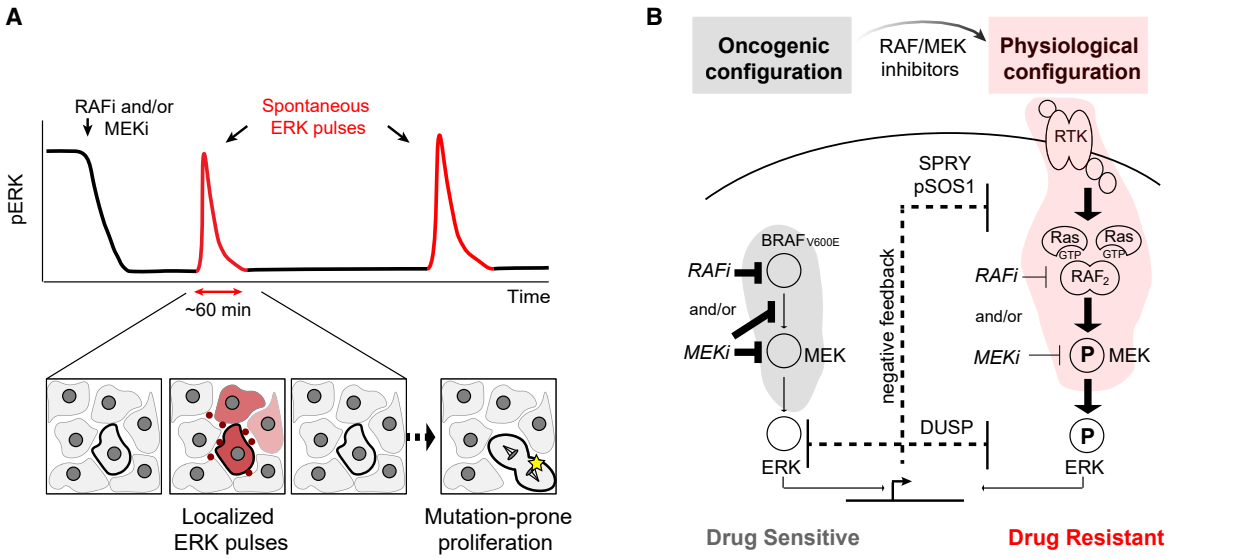

Figure 7. Differential Inhibition of Oncogenic and Physiological MAPK Signaling and Persistence of BRAF-Mutant Melanoma Cells through Spontaneous Receptor-Driven ERK Pulses

(A) Schematic of spontaneous RTK-mediated ERK pulses that promote slow proliferation of $BRAF^{V600E}$ melanoma cells in which oncogenic MAPK signaling is profoundly inhibited by RAF and/or MEK inhibitors.

(B) Presence in $BRAF^{V600E}$ melanoma cells of two different configurations of the MAPK signaling cascade. The oncogenic configuration inhibits activation of the physiological configuration through negative feedback regulators such as DUSPs, SPRY proteins and phosphorylation of SOS1. When the drugs are present and $BRAF^{V600E}$ signaling is inhibited, the levels of negative regulators fall, allowing the physiological configuration, which is resistant to both RAF and MEK inhibitors, to transduce growth factor signals operating in a paracrine/autocrine manner.

DISCUSSION

In this paper we show that $BRAF^{V600E}$ melanoma cells exposed to RAF and MEK inhibitors experience sporadic pulses of high ERK activity that are sufficient to promote cell survival and division, thereby generating slowly dividing, drug-adapted "persister" cells (this state is also known as adaptive or non-genetic drug resistance). In xenografted tumors treated with RAF/MEK inhibitors, clusters of pERK-high cells are evident by histology, and intravital imaging reveals pulsatile ERK activation. Further work will be required to show that the underlying mechanisms and consequences of pulsing are similar in cultured cells and tumors, but our data strongly suggest that the rebound in ERK activity previously observed in pre-clinical studies and patient samples (Lito et al., 2012) involves sporadic, strong pulses of ERK activity in single cells rather than a low level of sustained ERK reactivation. The sensitivity of ERK pulsing to RTK inhibition, the occurrence of pulsing in local patches of cells, and wave-like propagation of pulses suggest the involvement of paracrine/autocrine signaling (Figure 7A).

In the drug-adapted state, which can persist for weeks in culture (Fallahi-Sichani et al., 2017; Paudel et al., 2018; Shaffer et al., 2017; Yang et al., 2020), sustained ERK pulsing drives slow proliferation. However, viable cell number remains approximately constant because the number of newly born cells balances the number of dying cells. We find that, under these conditions, dividing cells experience replication stress and express the error-prone polymerases previously proposed to facilitate emergence of clones carrying resistance mutations (Russo et al., 2019; Cipponi et al., 2020). Thus, continued survival and division of persister cells may promote genetically encoded resistance in melanoma, but direct measurement of mutation frequency will be required to test this hypothesis.

Receptor-Driven Pulses and Chronic $BRAF^{V600E}$ Signaling Involve Distinct MAPK Configurations with Different Sensitivity to RAF and MEK Inhibitors

Experiments and computational modeling show that ERK pulsing is possible because MAPK signaling in $BRAF^{V60OE}$ cells can operate in two distinct configurations (Figure 7B). The oncogenic configuration driven by $BRAF^{V600E}$ monomers chronically activates ERK and is highly sensitive to RAF and MEK inhibitors. When the oncogenic configuration is inhibited, negative feedback on receptors is relieved. This enables a switch to a second latent "physiological" configuration involving RTKs, downstream Ras-GTP and BRAF/CRAF dimers. This configuration is responsive to factors in the local microenvironment and is resistant to both RAF and MEK inhibitors. As a result, these drugs potentiate MAPK signaling driven by transmembrane receptors under conditions in which the drugs block oncogenic signaling. Given the dependency of BRAF-mutant melanomas on MAPK activity (Long et al., 2014), it seems likely that the presence of the latent physiological configuration represents a key limitation in RAF/MEK therapy. It might therefore seem logical to target growth factors to improve therapeutic response. However, multiple receptors (e.g., ERBB1/2, c-MET, and FGFR) (Straussman et al., 2012; Wilson et al., 2012) are individually capable of inducing ERK pulsing when cognate ligands are present. This likely explains why blocking RTKs with selective drugs has not proven broadly effective in overcoming drug resistance in melanoma (Ahmed and Haass, 2018).

Although RTK-driven ERK pulsing promotes persistence, pulsing is insufficient for rapid growth of $BRAF^{V600E}$ tumors: otherwise, RAF/MEK inhibitors would not be effective as anticancer drugs. This contrast with EGFR signaling in colorectal cancer, which can be targeted therapeutically (e.g., with cetuximab) and which is a primary contributor to RAF inhibitors resistance (combined inhibition of BRAF and EGFR is an FDA-approved therapy for $BRAF^{V600E}$ colorectal cancers [Kopetz et al., 2019; Prahallad et al., 2012]). We propose that persistence in drug-adapted melanoma cells and primary resistance in cancers expressing abundant RTKs (e.g., EGFR in colorectal cancers) differ primarily in the duration of ERK activation: sporadic pulsing is sufficient for persistence but chronic or frequent signaling is necessary for tumor growth.

In our studies, spontaneous ERK pulses likely arise from localized release of growth factors enhanced by non-uniform distribution of RTKs at a single-cell level (Shaffer et al., 2017; Spencer et al., 2009). Once RTKs bind ligand, receptors are efficiently endocytosed and either degraded or recycled, terminating signaling and setting up the MAPK cascade for a subsequent pulse. These pulses superficially resemble the waves of MAPK activity that maintain tissue homeostasis in normal skin (Hiratsuka et al., 2015; Muta et al., 2019; Hiratsuka et al., 2020). Heterogeneous expression of EGFR and AXL has also been associated with drug resistance in patients (Tirosh et al., 2016; Shaffer et al., 2017). Live-cell movies suggest that dying cells are another likely source of autocrine/paracrine signals, possibly including presentation of the AXL ligand Gas6 in the context of phosphatidylserine lipids (Müller et al., 2014). When induced by exogenous ligand addition, an ERK pulse is sufficient to induce expression of genes necessary for cell-cycle progression such as cyclin D (Zwang et al., 2011). However, the relationship between pulsing and cell division in single cells is probabilistic, and it remains unknown why multiple pulses precede division in some cells but not others (Albeck et al., 2013; Aoki et al., 2013). It seems likely that other signaling cascades downstream of receptors might contribute to the decision to divide (e.g., those involving JNK or AKT) (Fallahi-Sichani et al., 2015; Yang et al., 2020).

Lower Potency of RAF and MEK Inhibitors for Receptor Signaling Enables Adaptive Resistance but Might Be Their Saving Grace with Respect to Tolerability

A key rationale for combining MEK inhibitors with RAF inhibitors is to prevent all forms of MAPK reactivation (Chapman et al., 2014). However, we find that MEK inhibitors such as trametinib and cobimetinib are unexpectedly ~50- to 100-fold less potent on receptor-mediated MAPK signaling than on oncogenic signaling, making them unable to inhibit ERK pulsing at clinically accessible doses. Our computational model shows that multiple biochemical mechanisms, including the resistance of RAF dimers downstream of RTKs to RAF inhibitors, the ability of MEK inhibitors to block MEK phosphorylation by monomeric $BRAF^{V600E}$, but not dimeric RAF, and the higher affinity of MEK inhibitors for unphosphorylated MEK are all involved in creating a wide dose range over which combined RAF and MEK inhibitors suppress oncogenic signaling but potentiate receptor-driven ERK pulsing (the physiological configuration in Figure 7B).

Could new drugs or drug combinations be deployed to block pulsatile MAPK signaling and the emergence of persister cells? Drugs able to inhibit the physiological and oncogenic MAPK configurations with similar potency, such as pan-RAF inhibitors (Peng et al., 2015) or MEK inhibitors blocking MEK phosphorylation by RAF dimers, are a possibility. However, we speculate that the resistance of physiological MAPK signaling to both RAF and MEK inhibitors might explain why these drugs spare normal cells and are well tolerated in patients (Chapman et al., 2011; Flaherty et al., 2012). The Achilles heel of RAF and MEK inhibitors with respect to adaptive resistance might therefore be their saving grace with respect to tolerability. If so, the key to more durable therapy lies not in deeper inhibition of the core MAPK cascade, which might be toxic to non-transformed cells, but rather the identification of vulnerabilities specific to the persister state. This will benefit from better understanding of this state (Shaffer et al., 2017) and whether persister cells have recurrent features or vulnerabilities that can be targeted therapeutically (Schuh et al., 2020). These might include proteins downstream of multiple growth factor receptors (e.g., SHP2) (Chen et al., 2016), accumulation of DNA damage (Margue et al., 2019), or dependence on specific survival pathways (Coppé et al., 2019; Fallahi-Sichani et al., 2015; Hangauer et al., 2017).

Limitations of Study

This study focuses on a single, widely studied melanoma cell line (A375) that is well suited to long-term live-cell imaging and efficiently forms xenografts. We find evidence of rare, sporadic MAPK reactivation in seven additional BRAF-mutant melanoma cell lines treated with RAF and MEK inhibitors but have not yet performed live-cell imaging to prove that this involves ERK pulsing. Intravital imaging studies are consistent with pulsing, but technical limitations (~4.5-h maximum for movies in xenografts) made it impossible to link ERK pulses to proliferation. While it may be possible to obtain fixed-cell data on different MAPK configurations in actual human tumors, live-cell studies of on-treatment tumors are impossible given current technology. Our data strongly implicate RTKs and autocrine/paracrine signaling in pulsing, and dead cell bodies may express the AXL ligand Gas6 in an active form, but the involvement of multiple growth factors in generating ERK pulses makes it difficult to demonstrate a role for any single ligand. For simplicity, we have focused mechanistic modeling on the protypical autocrine ligand EGF, even though this might not be the only relevant ligand in human tumors. Computational modeling as performed in this study provides a sufficient explanation for MAPK activity in the presence of MEK or RAF inhibitors, but it does not exclude additional mechanisms (e.g., MEK and ERK dimerization or binding to KSR scaffolds). Our use of an extensible rule-based modeling framework will facilitate future study of additional mechanisms.

STAR★METHODS

Detailed methods are provided in the online version of this paper and include the following:

- KEY RESOURCES TABLE
- RESOURCE AVAILABILITY
  - Lead Contact

SUPPLEMENTAL INFORMATION

Supplemental Information can be found online at https://doi.org/10.1016/j.cels.2020.10.002.

ACKNOWLEDGMENTS

We thank S. Boswell, A. Sokolov, Z. Maliga, C. Yapp, M. Chung, M. Fallahi-Sichani, M. Rogava, I. Gasic, and R. Madsen for their help, as well as G. Lahav and the Nikon Imaging Center at HMS for assistance with microscopy and the O2 High Performance Compute Cluster for computing support. The work was funded primarily by NCI grant U54-CA225088 (P.K.S.) and by U54-CA210180 (D.A.L.), U01-CA227544 (W.-J.Q. and H.S.W.), P41-GM103493 (T.S., L.Y., and C.D.N.), R00-CA207744 (M.A.M.) and U01-CA206997 (R.W.), a Novartis Foundation fellowship to L.G., HFSP grant LT000259/2019-L1 to F.F., and a SNSF Early Postdoc Mobility fellowship P2ZHP3_181475 to D.S. Proteomics was performed at EMSL, a national scientific user facility sponsored by the DOE under contract DE-AC05-76RL0 1830.

AUTHOR CONTRIBUTIONS

L.G. conceived and designed the study; P.K.S. supervised the work. L.G., C.C., G.S., S.K.L., J.M., S.V., L.A.C., J.-Y.C., M.I.A., G.J.B., and D.S. generated reagents and performed experiments. L.G. performed data analysis. L.G. and F.F. performed model analysis. A.C. and D.A.L. performed receptor quantification. D.L., T.S., L.Y., C.D.N., W.-J.Q., and H.S.W. performed proteomics studies. T.N., R.H.K., R.W., and M.A.M. performed intravital imaging studies. L.G. and P.K.S. wrote the manuscript. All authors reviewed and approved the final version.

DECLARATION OF INTERESTS

P.K.S. is a member of the SAB or BOD of Glencoe Software, Applied Biomath, and RareCyte and has equity in these companies and is on the SAB of and NanoString. In the last five years the Sorger lab has received research funding from Novartis and Merck. P.K.S. declares that none of these relationships are directly or indirectly related to the content of this manuscript. R.W. is a co-founder of T2Biosystems and Lumicell, serves as a scientific advisor for ModeRNA Therapeutics, Tarveda Therapeutics, and Alivio Therapeutics. None of these activities are related to the manuscript. The other authors declare that they have no competing interests.

Received: July 23, 2019
Revised: July 21, 2020
Accepted: October 3, 2020
Published: October 27, 2020

REFERENCES

Ahmed, F., and Haass, N.K. (2018). Microenvironment-driven dynamic heterogeneity and phenotypic plasticity as a mechanism of melanoma therapy resistance. Front. Oncol. *8*, 173.

Albeck, J.G., Mills, G.B., and Brugge, J.S. (2013). Frequency-modulated pulses of ERK activity transmit quantitative proliferation signals. Mol. Cell *49*, 249–261.

Aoki, K., Kumagai, Y., Sakurai, A., Komatsu, N., Fujita, Y., Shionyu, C., and Matsuda, M. (2013). Stochastic ERK activation induced by noise and cell-to-cell propagation regulates cell density-dependent proliferation. Mol. Cell *52*, 529–540.

Cappell, S.D., Chung, M., Jaimovich, A., Spencer, S.L., and Meyer, T. (2016). Irreversible APC(Cdh1) inactivation underlies the point of no return for cell-cycle entry. Cell *166*, 167–180.

Carver, B.S., Chapinski, C., Wongvipat, J., Hieronymus, H., Chen, Y., Chandarlapaty, S., Arora, V.K., Le, C., Koutcher, J., Scher, H., et al. (2011). Reciprocal feedback regulation of PI3K and androgen receptor signaling in PTEN-deficient prostate cancer. Cancer Cell *19*, 575–586.

Chandarlapaty, S. (2012). Negative feedback and adaptive resistance to the targeted therapy of cancer. Cancer Discov. *2*, 311–319.

Chapman, P.B., Hauschild, A., Robert, C., Haanen, J.B., Ascierto, P., Larkin, J., Dummer, R., Garbe, C., Testori, A., Maio, M., et al. (2011). Improved survival with vemurafenib in melanoma with BRAF V600E mutation. N. Engl. J. Med. *364*, 2507–2516.

Chapman, P.B., Solit, D.B., and Rosen, N. (2014). Combination of RAF and MEK inhibition for the treatment of BRAF-mutated melanoma: feedback is not encouraged. Cancer Cell *26*, 603–604.

Chen, Y.N., LaMarche, M.J., Chan, H.M., Fekkes, P., Garcia-Fortanet, J., Acker, M.G., Antonakos, B., Chen, C.H.-T., Chen, Z., Cooke, V.G., et al. (2016). Allosteric inhibition of SHP2 phosphatase inhibits cancers driven by receptor tyrosine kinases. Nature *535*, 148–152.

Cipponi, A., Goode, D.L., Bedo, J., McCabe, M.J., Pajic, M., Croucher, D.R., Rajal, A.G., Junankar, S.R., Saunders, D.N., Lobachevsky, P., et al. (2020). MTOR signaling orchestrates stress-induced mutagenesis, facilitating adaptive evolution in cancer. Science *368*, 1127–1131.

Claas, A.M., Atta, L., Gordonov, S., Meyer, A.S., and Lauffenburger, D.A. (2018). Systems modeling identifies divergent receptor tyrosine kinase reprogramming to MAPK pathway inhibition. Cell. Mol. Bioeng. *11*, 451–469.

Coppé, J.P., Mori, M., Pan, B., Yau, C., Wolf, D.M., Ruiz-Saenz, A., Brunen, D., Prahallad, A., Cornelissen-Steijger, P., Kemper, K., et al. (2019). Mapping phospho-catalytic dependencies of therapy-resistant tumours reveals actionable vulnerabilities. Nat. Cell Biol. *21*, 778–790.

Fallahi-Sichani, M., Becker, V., Izar, B., Baker, G.J., Lin, J.R., Boswell, S.A., Shah, P., Rotem, A., Garraway, L.A., and Sorger, P.K. (2017). Adaptive resistance of melanoma cells to RAF inhibition via reversible induction of a slowly dividing de-differentiated state. Mol. Syst. Biol. *13*, 905.

Fallahi-Sichani, M., Moerke, N.J., Niepel, M., Zhang, T., Gray, N.S., and Sorger, P.K. (2015). Systematic analysis of BRAF(V600E) melanomas reveals a role for JNK/c-Jun pathway in adaptive resistance to drug-induced apoptosis. Mol. Syst. Biol. *11*, 797.

Flaherty, K.T., Robert, C., Hersey, P., Nathan, P., Garbe, C., Milhem, M., Demidov, L.V., Hassel, J.C., Rutkowski, P., Mohr, P., et al. (2012). Improved survival with MEK inhibition in BRAF-mutated melanoma. N. Engl. J. Med. *367*, 107–114.

Freeman, A.K., Ritt, D.A., and Morrison, D.K. (2013). Effects of Raf dimerization and its inhibition on normal and disease-associated Raf signaling. Mol. Cell *49*, 751–758.

Fröhlich, F., Kaltenbacher, B., Theis, F.J., and Hasenauer, J. (2017). Scalable parameter estimation for genome-scale biochemical reaction networks. PLoS Computational Biology *13*, e1005331.

Goel, S., Wang, Q., Watt, A.C., Tolaney, S.M., Dillon, D.A., Li, W., Ramm, S., Palmer, A.C., Yuzugullu, H., Varadan, V., et al. (2016). Overcoming therapeutic resistance in HER2-positive breast cancers with CDK4/6 inhibitors. Cancer Cell *29*, 255–269.

Groenendijk, F.H., and Bernards, R. (2014). Drug resistance to targeted therapies: déjà vu all over again. Mol. Oncol. *8*, 1067–1083.

Hangauer, M.J., Viswanathan, V.S., Ryan, M.J., Bole, D., Eaton, J.K., Matov, A., Galeas, J., Dhruv, H.D., Berens, M.E., Schreiber, S.L., et al. (2017). Drug-tolerant persister cancer cells are vulnerable to GPX4 inhibition. Nature *551*, 247–250.

Hatzivassiliou, G., Haling, J.R., Chen, H., Song, K., Price, S., Heald, R., Hewitt, J.F.M., Zak, M., Peck, A., Orr, C., et al. (2013). Mechanism of MEK inhibition determines efficacy in mutant KRAS- versus BRAF-driven cancers. Nature *501*, 232–236.

Hiratsuka, T., Bordeu, I., Pruessner, G., and Watt, F.M. (2020). Regulation of ERK basal and pulsatile activity control proliferation and exit from the stem cell compartment in mammalian epidermis. Proc. Natl. Acad. Sci. *117*, 17796.

Hiratsuka, T., Fujita, Y., Naoki, H., Aoki, K., Kamioka, Y., and Matsuda, M. (2015). Intercellular propagation of extracellular signal-regulated kinase activation revealed by in vivo imaging of mouse skin. eLife *4*, e05178.

Kholodenko, B.N. (2015). Drug resistance resulting from kinase dimerization is rationalized by thermodynamic factors describing allosteric inhibitor effects. Cell Rep. *12*, 1939–1949.

Kim, D., Langmead, B., and Salzberg, S.L. (2015). HISAT: a fast spliced aligner with low memory requirements. Nat. Methods *12*, 357–360.

Kopetz, S., Grothey, A., Yaeger, R., Van Cutsem, E., Desai, J., Yoshino, T., Wasan, H., Ciardiello, F., Loupakis, F., Hong, Y.S., et al. (2019). Encorafenib, binimetinib, and cetuximab in BRAF V600E–mutated colorectal cancer. N. Engl. J. Med. *381*, 1632–1643.

Köster, J., and Rahmann, S. (2012). Snakemake–a scalable bioinformatics workflow engine. Bioinformatics *28*, 2520–2522.

Lamprecht, M.R., Sabatini, D.M., and Carpenter, A.E. (2007). CellProfiler: free, versatile software for automated biological image analysis. BioTechniques *42*, 71–75.

Lao, D.H., Chandramouli, S., Yusoff, P., Fong, C.W., Saw, T.Y., Tai, L.P., Yu, C.Y., Leong, H.F., and Guy, G.R. (2006). A Src homology 3-binding sequence on the C terminus of Sprouty2 is necessary for inhibition of the Ras/ERK pathway downstream of fibroblast growth factor receptor stimulation. J. Biol. Chem. *281*, 29993–30000.

Lin, J.R., Izar, B., Wang, S., Yapp, C., Mei, S., Shah, P.M., Santagata, S., and Sorger, P.K. (2018). Highly multiplexed immunofluorescence imaging of human tissues and tumors using t-CyCIF and conventional optical microscopes. eLife *7*, e31657.

Lito, P., Pratilas, C.A., Joseph, E.W., Tadi, M., Halilovic, E., Zubrowski, M., Huang, A., Wong, W.L., Callahan, M.K., Merghoub, T., et al. (2012). Relief of profound feedback inhibition of mitogenic signaling by RAF inhibitors attenuates their activity in BRAFV600E melanomas. Cancer Cell *22*, 668–682.

Lito, P., Saborowski, A., Yue, J., Solomon, M., Joseph, E., Gadal, S., Saborowski, M., Kastenhuber, E., Fellmann, C., Ohara, K., et al. (2014). Disruption of CRAF-mediated MEK activation is required for effective MEK inhibition in KRAS mutant tumors. Cancer Cell *25*, 697–710.

Long, G.V., Fung, C., Menzies, A.M., Pupo, G.M., Carlino, M.S., Hyman, J., Shahheydari, H., Tembe, V., Thompson, J.F., Saw, R.P., et al. (2014). Increased MAPK reactivation in early resistance to dabrafenib/trametinib combination therapy of BRAF-mutant metastatic melanoma. Nat. Commun. *5*, 5694.

Lopez, C.F., Muhlich, J.L., Bachman, J.A., and Sorger, P.K. (2013). Programming biological models in Python using PySB. Mol. Syst. Biol. *9*, 646.

MacLean, B., Tomazela, D.M., Shulman, N., Chambers, M., Finney, G.L., Frewen, B., Kern, R., Tabb, D.L., Liebler, D.C., and MacCoss, M.J. (2010). Skyline: an open source document editor for creating and analyzing targeted proteomics experiments. Bioinformatics *26*, 966–968.

Margue, C., Philippidou, D., Kozar, I., Cesi, G., Felten, P., Kulms, D., Letellier, E., Haan, C., and Kreis, S. (2019). Kinase inhibitor library screening identifies synergistic drug combinations effective in sensitive and resistant melanoma cells. J. Exp. Clin. Cancer Res. *38*, 56.

Montero-Conde, C., Ruiz-Llorente, S., Dominguez, J.M., Knauf, J.A., Viale, A., Sherman, E.J., Ryder, M., Ghossein, R.A., Rosen, N., and Fagin, J.A. (2013). Relief of feedback inhibition of *HER3* transcription by RAF and MEK inhibitors attenuates their antitumor effects in *BRAF* -Mutant thyroid carcinomas. Cancer Discov. *3*, 520–533.

Müller, J., Krijgsman, O., Tsoi, J., Robert, L., Hugo, W., Song, C., Kong, X., Possik, P.A., Cornelissen-Steijger, P.D.M., Geukes Foppen, M.H.G., et al. (2014). Low MITF/AXL ratio predicts early resistance to multiple targeted drugs in melanoma. Nat. Commun. *5*, 5712.

Muta, Y., Matsuda, M., and Imajo, M. (2019). Divergent dynamics and functions of ERK MAP kinase signaling in development, homeostasis and cancer: lessons from fluorescent bioimaging. Cancers *11*, 513.

Niederst, M.J., and Engelman, J.A. (2013). Bypass mechanisms of resistance to receptor tyrosine kinase inhibition in lung cancer. Sci. Signal. *6*, re6.

Paudel, B.B., Harris, L.A., Hardeman, K.N., Abugable, A.A., Hayford, C.E., Tyson, D.R., and Quaranta, V. (2018). A nonquiescent "idling" population state in drug-treated, BRAF-mutated melanoma. Biophys. J. *114*, 1499–1511.

Pazarentzos, E., and Bivona, T.G. (2015). Adaptive stress signaling in targeted cancer therapy resistance. Oncogene *34*, 5599–5606.

Peng, S.B., Henry, J.R., Kaufman, M.D., Lu, W.P., Smith, B.D., Vogeti, S., Rutkoski, T.J., Wise, S., Chun, L., Zhang, Y., et al. (2015). Inhibition of RAF isoforms and active dimers by LY3009120 leads to anti-tumor activities in RAS or BRAF mutant cancers. Cancer Cell *28*, 384–398.

Prahallad, A., Sun, C., Huang, S., Di Nicolantonio, F., Salazar, R., Zecchin, D., Beijersbergen, R.L., Bardelli, A., and Bernards, R. (2012). Unresponsiveness of colon cancer to BRAF(V600E) inhibition through feedback activation of EGFR. Nature *483*, 100–103.

Pratilas, C.A., Taylor, B.S., Ye, Q., Viale, A., Sander, C., Solit, D.B., and Rosen, N. (2009). V600EBRAF is associated with disabled feedback inhibition of RAF-MEK signaling and elevated transcriptional output of the pathway. Proc. Natl. Acad. Sci. USA *106*, 4519–4524.

Ramirez, M., Rajaram, S., Steininger, R.J., Osipchuk, D., Roth, M.A., Morinishi, L.S., Evans, L., Ji, W., Hsu, C.-H., Thurley, K., et al. (2016). Diverse drug-resistance mechanisms can emerge from drug-tolerant cancer persister cells. Nat. Commun. *7*, 10690.

Rauch, N., Rukhlenko, O.S., Kolch, W., and Kholodenko, B.N. (2016). MAPK kinase signalling dynamics regulate cell fate decisions and drug resistance. Curr. Opin. Struct. Biol. *41*, 151–158.

Regot, S., Hughey, J.J., Bajar, B.T., Carrasco, S., and Covert, M.W. (2014). High-sensitivity measurements of multiple kinase activities in live single cells. Cell *157*, 1724–1734.

Resat, H., Ewald, J.A., Dixon, D.A., and Wiley, H.S. (2003). An integrated model of epidermal growth factor receptor trafficking and signal transduction. Biophys. J. *85*, 730–743.

Reyes, J., Chen, J.-Y., Stewart-Ornstein, J., Karhohs, K.W., Mock, C.S., and Lahav, G. (2018). Fluctuations in p53 signaling allow escape from cell-cycle arrest. Mol. Cell *71*, 581–591.e5.

Rukhlenko, O.S., Khorsand, F., Krstic, A., Rozanc, J., Alexopoulos, L.G., Rauch, N., Erickson, K.E., Hlavacek, W.S., Posner, R.G., Gómez-Coca, S., et al. (2018). Dissecting RAF inhibitor resistance by structure-based modeling reveals ways to overcome oncogenic RAS signaling. Cell Syst. *7*, 161–179.e14.

Russo, M., Crisafulli, G., Sogari, A., Reilly, N.M., Arena, S., Lamba, S., Bartolini, A., Amodio, V., Magrì, A., Novara, L., et al. (2019). Adaptive mutability of colorectal cancers in response to targeted therapies. Science *366*, 1473–1480.

Saha, M., Carriere, A., Cheerathodi, M., Zhang, X., Lavoie, G., Rush, J., Roux, P.P., and Ballif, B.A. (2012). RSK phosphorylates SOS1 creating 14-3-3-docking sites and negatively regulating MAPK activation. Biochem. J. *447*, 159–166.

Schapiro, D., Jackson, H.W., Raghuraman, S., Fischer, J.R., Zanotelli, V.R.T., Schulz, D., Giesen, C., Catena, R., Varga, Z., and Bodenmiller, B. (2017). histoCAT: analysis of cell phenotypes and interactions in multiplex image cytometry data. Nat. Methods *14*, 873–876.

Schuh, L., Saint-Antoine, M., Sanford, E.M., Emert, B.L., Singh, A., Marr, C., Raj, A., and Goyal, Y. (2020). Gene networks with transcriptional bursting recapitulate rare transient coordinated high expression states in cancer. Cell Syst. *10*, 363–378.e12.

Sekar, J.A.P., Hogg, J.S., and Faeder, J.R. (2017). Energy-based modeling in BioNetGen. In Proceedings - 2016 IEEE International Conference on Bioinformatics and Biomedicine, BIBM 2016, pp. 1460–1467.

Shaffer, S.M., Dunagin, M.C., Torborg, S.R., Torre, E.A., Emert, B., Krepler, C., Beqiri, M., Sproesser, K., Brafford, P.A., Xiao, M., et al. (2017). Rare cell variability and drug-induced reprogramming as a mode of cancer drug resistance. Nature *546*, 431–435.

Shi, T., Niepel, M., McDermott, J.E., Gao, Y., Nicora, C.D., Chrisler, W.B., Markillie, L.M., Petyuk, V.A., Smith, R.D., Rodland, K.D., et al. (2016). Conservation of protein abundance patterns reveals the regulatory architecture of the EGFR-MAPK pathway. Sci. Signal. *9*, rs6.

Shi, T., Quek, S.I., Gao, Y., Nicora, C.D., Nie, S., Fillmore, T.L., Liu, T., Rodland, K.D., Smith, R.D., Leach, R.J., et al. (2017). Multiplexed targeted mass spectrometry assays for prostate cancer-associated urinary proteins. Oncotarget *8*, 101887–101898.

Sommer, C., Straehle, C., Köthe, U., and Hamprecht, F.A. (2011). ilastik: interactive learning and segmentation toolkit. In Eighth IEEE International Symposium on Biomedical Imaging (ISBI) (Proceedings (2011)), pp. 230–233.

Spencer, S.L., Gaudet, S., Albeck, J.G., Burke, J.M., and Sorger, P.K. (2009). Non-genetic origins of cell-to-cell variability in TRAIL-induced apoptosis. Nature *459*, 428–432.

Stapor, P., Weindl, D., Ballnus, B., Hug, S., Loos, C., Fiedler, A., Krause, S., Hroß, S., Fröhlich, F., and Hasenauer, J. (2018). PESTO: parameter EStimation TOolbox. Bioinformatics *34*, 705–707.

Straussman, R., Morikawa, T., Shee, K., Barzily-Rokni, M., Qian, Z.R., Du, J., Davis, A., Mongare, M.M., Gould, J., Frederick, D.T., et al. (2012). Tumour micro-environment elicits innate resistance to RAF inhibitors through HGF secretion. Nature *487*, 500–504.

Sun, C., Wang, L., Huang, S., Heynen, G.J.J.E., Prahallad, A., Robert, C., Haanen, J., Blank, C., Wesseling, J., Willems, S.M., et al. (2014). Reversible and adaptive resistance to BRAF(V600E) inhibition in melanoma. Nature *508*, 118–122.

Tirosh, I., Izar, B., Prakadan, S.M., Wadsworth, M.H., Treacy, D., Trombetta, J.J., Rotem, A., Rodman, C., Lian, C., Murphy, G., et al. (2016). Dissecting the multicellular ecosystem of metastatic melanoma by single-cell RNA-seq. Science *352*, 189–196.

Wilson, T.R., Fridlyand, J., Yan, Y., Penuel, E., Burton, L., Chan, E., Peng, J., Lin, E., Wang, Y., Sosman, J., et al. (2012). Widespread potential for growth-factor-driven resistance to anticancer kinase inhibitors. Nature *487*, 505–509.

Yang, H.W., Cappell, S.D., Jaimovich, A., Liu, C., Chung, M., Daigh, L.H., Pack, L.R., Fan, Y., Regot, S., Covert, M., et al. (2020). Stress-mediated exit to quiescence restricted by increasing persistence in CDK4/6 activation. ELife *9*, e44571.

Yang, C., Tian, C., Hoffman, T.E., Jacobsen, N.K., and Spencer, S.L. (2020a). Rapidly induced drug adaptation mediates escape from BRAF inhibition in single melanoma cells. BioRxiv 2020.03.15.992982.

Yao, Z., Torres, N.M., Tao, A., Gao, Y., Luo, L., Li, Q., de Stanchina, E., Abdel-Wahab, O., Solit, D.B., Poulikakos, P.I., and Rosen, N. (2015). BRAF mutants evade ERK-dependent feedback by different mechanisms that determine their sensitivity to pharmacologic inhibition. Cancer Cell *28*, 370–383.

Yi, L., Shi, T., Gritsenko, M.A., X'avia Chan, C.Y., Fillmore, T.L., Hess, B.M., Swensen, A.C., Liu, T., Smith, R.D., Wiley, H.S., and Qian, W.-J. (2018). Targeted quantification of phosphorylation dynamics in the context of EGFR-MAPK pathway. Anal. Chem. *90*, 5256–5263.

Zwang, Y., Sas-Chen, A., Drier, Y., Shay, T., Avraham, R., Lauriola, M., Shema, E., Lidor-Nili, E., Jacob-Hirsch, J., Amariglio, N., et al. (2011). Two phases of mitogenic signaling unveil roles for p53 and EGR1 in elimination of inconsistent growth signals. Mol. Cell *42*, 524–535.

STAR★METHODS

KEY RESOURCES TABLE

REAGENT or RESOURCE	SOURCE	IDENTIFIER
Antibodies		
Phospho-p44/42 MAPK (Erk1/2) (Thr202/Tyr204) antibody	Cell Signaling Technology	Cat# 4370, RRID: AB_2315112
Phospho-MEK1/2 (Ser217/221) antibody	Cell Signaling Technology	Cat# 9121, RRID: AB_331648
Phospho-p90RSK (Thr359) (D1E9) antibody	Cell Signaling Technology	Cat# 8753, RRID: AB_2783561
Phospho-S6 Ribosomal Protein (Ser240/244) (D68F8) XP Rabbit mAb (Alexa Fluor 488 Conjugate) antibody	Cell Signaling Technology	Cat# 5018, RRID: AB_10695861
Phospho-S6 Ribosomal Protein (Ser235/236) (D57.2.2E) XP Rabbit mAb (Alexa Fluor 555 Conjugate) antibody	Cell Signaling Technology	Cat# 3985, RRID: AB_10693792
EGFR Monoclonal Antibody (199.12)	Thermo Fisher Scientific	Cat# MA5-13319, RRID: AB_10985841
Alexa Fluor 647, Donkey anti-Rabbit IgG (H+L) Secondary Antibody	Thermo Fisher Scientific	Cat# A-31573, RRID: AB_2536183
Alexa Fluor 488, Donkey anti-Mouse IgG (H+L) Secondary Antibody	Thermo Fisher Scientific	Cat# A21202, RRID: AB_141607
EGF Receptor (D38B1) XP Rabbit mAb	Cell Signaling Technology	Cat# 4267, RRID: AB_2246311
phospho-γH2AX (Ser139) rabbit mAb	Cell Signaling Technology	Cat# 9718, RRID: AB_2118009
Axl (C89E7) Rabbit mAb	Cell Signaling Technology	Cat# 8661, RRID: AB_11217435
c-Met (D1C2) Rabbit mAb	Cell Signaling Technology	Cat# 8198, RRID: AB_10858224
β-Actin Antibody (C4)	Santa Cruz Biotechnology	Cat# sc-47778, RRID: AB_2714189
Anti-rabbit IgG, HRP-linked Antibody	Cell Signaling Technology	Cat# 7074, RRID: AB_2099233
Anti-mouse IgG, HRP-linked Antibody	Cell Signaling Technology	Cat# 7076, RRID: AB_330924
Biological Samples		
A375 Xenograft Formalin-Fixed Paraffin-Embedded (FFPE) tissue slides	Fallahi-Sichani et al., 2017	N/A
Chemicals, Peptides, and Recombinant Proteins		
Vemurafenib, RAF inhibitor	MedChem Express	Cat# HY-12057
Dabrafenib, RAF inhibitor	MedChem Express	Cat# HY-14660
PLX8394, RAF inhibitor	MedChem Express	Cat# HY-18972
LY3009120, RAF inhibitor	MedChem Express	Cat# HY-12558
AZ628, RAF inhibitor	MedChem Express	Cat# HY-11004
Cobimetinib, MEK inhibitor	MedChem Express	Cat# HY-13064
Trametinib, MEK inhibitor	MedChem Express	Cat# HY-10999
Selumetinib, MEK inhibitor	MedChem Express	Cat# HY-50706
Binimetinib, MEK inhibitor	MedChem Express	Cat# HY-15202
PD0325901, MEK inhibitor	MedChem Express	Cat# HY-10254
Lapatinib, ERBB inhibitor	MedChem Express	Cat# HY-50898
Erlotinib, ERBB inhibitor	MedChem Express	Cat# HY-50896
SHP099, SHP2 inhibitor	MedChem Express	Cat# HY-100388
R248, AXL inhibitor	MedChem Express	Cat# HY-15150
Infingratinib (BGJ398), FGFR inhibitor	Active Biochem	Cat# A-1143
Recombinant Human EGF, growth factor	Peprotech	Cat# 100-15
Recombinant Human Heregulinβ-1, growth factor	Peprotech	Cat# 100-03
Recombinant Human FGF-8a, growth factor	Peprotech	Cat# 100-25A
Recombinant Human HGF, growth factor	Peprotech	Cat#100-39
EdU (5-ethynyl-2'-deoxyuridine)	Lumiprobe, Hunt Valley, MD	Cat# 10540

(*Continued on next page*)

Continued

REAGENT or RESOURCE	SOURCE	IDENTIFIER
Deposited Data		
Gene expression data (RNA seq) of A375 melanoma cells were deposited in the GEO (Gene Expression Omnibus) database: https://www.ncbi.nlm.nih.gov/geo/	GEO (Gene Expression Omnibus)	Accession number: GEO: GSE127988 Secure token for anonymous review: wvclkgmqddwpbqz
Protein abundance and phosphorylation data (SRM proteomics) were deposited in the Panorama public database at https://panoramaweb.org/labkey/	Panorama (Repository Software for Targeted Mass Spectrometry Assays from Skyline)	https://panoramaweb.org/fWeE7i.url Anonymous reviewer login info: Email: panorama+pnnl8@proteinms.net Password: %h4JDQCY
Processed datasets used to generate main and supplementary figures in the manuscript, provided as .csv files	Synapse database	https://www.synapse.org/#!Synapse:syn20551877/files/ Synapse ID: syn20551877 https://doi.org/10.7303/syn20551877. The repository is public.
Experimental Models: Cell Lines		
Human: A-375 (A375), Melanoma Cell Line	MGH Cancer Center, primary source ATCC	ATCC Cat# CRL-1619, RRID: CVCL_0132
Human:C32, Melanoma Cell Line	MGH Cancer Center, primary source ATCC	ATCC Cat# CRL-1585, RRID: CVCL_1097
Human: K2, Melanoma Cell Line	MGH Cancer Center, primary source ATCC	RRID: CVCL_AT85
Human: MMAc-SF (MMACSF), Melanoma Cell Line	MGH Cancer Center, primary source RIKEN BioResource Center	RCB Cat# RCB1200, RRID: CVCL_1420
Human: MZ-MEL-7 (MZ7MEL), Melanoma Cell Line	MGH Cancer Center, primary source Johannes Gutenberg University Mainz	RRID: CVCL_1436
Human: RVH-421 (RVH421), Melanoma Cell Line	MGH Cancer Center, primary source ATCC	RRID: CVCL_1672
Human: SKMEL28, Melanoma Cell Line	MGH Cancer Center, primary source ATCC	CLS Cat# 300337/p495_SK-MEL-28, RRID: CVCL_0526
Human: WM115, Melanoma Cell Line	MGH Cancer Center, primary source ATCC	ATCC Cat# CRL-1675, RRID: CVCL_0040
Human: HEK293T, Cell Line	ATCC	ATCC Cat# CRL-3216, RRID: CVCL_0063
A375_aEGFR1 (A375 with constitutive EGFR overexpression by CRISPRa; sgRNA1)	This work	N/A
A375_aEGFR2 (A375 with constitutive EGFR overexpression by CRISPRa; sgRNA2)	This work	N/A
A375_iEGFR (A375 with constitutive EGFR knockdown by CRISPRi; sgRNA1)	This work	N/A
A375 stably expressing polycistronic ERK-KTR:CFP, H2B:YFP and Geminin:RFP reporters	This work	N/A
Oligonucleotides		
See Table S2 for oligonucleotide sequences	This work	N/A
Recombinant DNA		
psPAX2	Addgene	Cat# 12260
pCMV-VSV-G	Addgene	Cat# 8454
pMH0001, expresses dCas9-BFP-KRAB, for CRISPRi	Addgene	Cat# 85969
pHRdSV40-dCas9-10xGCN4_v4-P2A-BFP, expresses dCas9 tagged with 10 copies of the GCN4 peptide v4 and BFP, for CRISPR a	Addgene	Cat# 60903

(*Continued on next page*)

Continued

REAGENT or RESOURCE	SOURCE	IDENTIFIER
pHRdSV40-scFv-GCN4-sfGFP-VP64-GB1-NLS, expresses an antibody that binds to the GCN4 peptide from the SunTag system, and is fused to VP64, for CRISPRa	Addgene	Cat# 60904
pU6-sgRNA EF1Alpha-puro-T2A-BFP	Addgene	Cat# 60955
4_pPB_ERKKTRmTq2_H2BVenus_mCherryGemin, fluorescent reporter for H2B(Venus), ERK:TTR (mTurquoise), Geminin (mCherry)	Fallahi-Sichani et al., 2017	N/A
pCMV_hyPBase	Fallahi-Sichani et al., 2017	N/A
Software and Algorithms		
PySB, open-source programming framework for Systems Biology modelling in Python	Lopez et al., 2013	http://pysb.org/
eBNG, energy-based modeling in BioNetGen	Sekar et al., 2017	https://github.com/RuleWorld/bionetgen
Amici (Advanced Multilanguage Interface to CVODES and IDAS) framework used for parameter estimation	Fröhlich et al., 2017	https://github.com/ICB-DCM/AMICI
Pypesto, a widely applicable and highly customizable toolbox for parameter estimation.	Stapor et al., 2018	http://snakemake.googlecode.com
Snakemake, workflow management system is a tool to create reproducible and scalable data analyses.	Köster and Rahmann, 2012	https://snakemake.readthedocs.io/en/stable/
Columbus, data storage and analysis system for high throughput microscopy software	PerkinElmer	http://www.perkinelmer.com/product/image-data-storage-and-analysis-system-columbus
Software for automatic segmentation, quantification and tracking fluorescent reporter cells live-cell imaging	Cappell et al., 2016	https://github.com/scappell/Cell_tracking
Software for manual tracking of cells	Reyes et al, 2018	https://github.com/balvahal/p53CinemaManual
Skyline software for analysis of proteomics samples	MacLean et al., 2010	https://skyline.ms/project/home/software/Skyline/begin.view
Ashlar for stitching and registration of cyclic microscopy images of large tissue sections	Muhlich et al., in preparation	https://github.com/labsyspharm/ashlar
Ilastik1.3.2, is a simple, user-friendly tool for interactive image classification, segmentation and analysis.	Sommer et al., 2011	https://www.ilastik.org/
CellProfiler3.1.8. is a free, open-source software to quantitatively measure phenotypes of images automatically.	Lamprecht et al., 2007	https://cellprofiler.org/
histoCAT, Histology Topography Cytometry Analysis Toolbox	Schapiro et al., 2017	https://github.com/BodenmillerGroup/histoCAT
Melanoma Adaptive Resistance Model (MARM1). Provided in SBML, BNG and PySB formats. Jupyter Notebooks are provided in a Docker container for the step-by-step construction and simulation of MARM1.	This work	https://github.com/labsyspharm/marm1-supplement
Other		
SuperSignal™ West Dura Extended Duration Substrate	Thermo Fisher Scientific	Cat# 34076
HCS CellMask™ Blue Stain	Thermo Fisher Scientific	Cat# 34076
Hoechst 33342	Invitrogen	Cat# H3570

RESOURCE AVAILABILITY

Lead Contact

Further information and requests for resources and reagents should be directed to and will be fulfilled by the Lead Contact, Peter Sorger (peter_sorger@hms.harvard.edu).

Materials Availability

Cell lines generated for this work are available upon request from the Lead Contact.

Data and Code Availability

- All experimental and simulation tabular datasets (.csv files) are available in the Synapse database (https://www.synapse.org/#!Synapse:syn20551877/files/, Synapse ID: syn20551877, https://doi.org/10.7303/syn20551877). Table S4 contains a description for each supplementary dataset.
- Gene expression data (RNA seq) are available at GEO (Gene Expression Omnibus, https://www.ncbi.nlm.nih.gov/geo/, accession number: GEO: GSE127988).
- The SRM proteomics data is available in the Panorama public database (https://panoramaweb.org/fWeE7i.url).
- The original code for constructing and running the MARM1 kinetic model is publicly available at GitHub (https://github.com/labsyspharm/marm1-supplement).
- The scripts used to generate the figures reported in this paper are available in the Synapse database (https://www.synapse.org/#!Synapse:syn20551877/files/, Synapse ID: syn20551877, https://doi.org/10.7303/syn20551877).
- Any additional information required to reproduce this work is available from the Lead Contact.

EXPERIMENTAL MODEL AND SUBJECT DETAILS

Cell Lines and Tissue Culture

Cell lines used in this study were obtained from the Massachusetts General Hospital Cancer Center and originated from the following primary sources: A375, C32, K2, RVH421, WM115, SKMEL28, and WM1552C (ATCC); MMACSF (RIKEN BioResource Center); and MZ7MEL (Johannes Gutenberg University Mainz). HEK293T was from ATCC. C32, K2, MMACSF, SKMEL28, RVH421, and WM115 cell lines were grown in DMEM/F12 (Invitrogen) supplemented with 5% heat inactivated fetal bovine serum (FBS) (Gibco) and 1% sodium pyruvate (Invitrogen). MZ7MEL and WM1552C were grown in RPMI-1640 (Corning) supplemented with 5% FBS and 1% sodium pyruvate (Invitrogen). A375 cells were grown in Dulbecco's modified eagle medium with 4.5 g/l D-glucose, 4 mM L-glutamine, and 1 mM sodium pyruvate (DMEM) (Corning), supplemented with 5% FBS. HEK293T cells were grown in DMEM supplemented with 10% FBS. Penicillin and streptomycin were added to all growth media at final concentrations of 100 U/mL and 100 μg/mL, respectively (Corning). Cells were tested for mycoplasma contamination using the MycoAlert mycoplasma detection kit (Lonza).

Xenografts for FFPE Imaging

Formalin-Fixed Paraffin-Embedded (FFPE) tissue slides of A375 xenografts were prepared as previously described (Fallahi-Sichani et al., 2017). Briefly, six-week-old NU/J mice (Jackson Laboratory, Stock# 002019) were injected subcutaneously in the right flank with 2.5 million A375 cells. Tumor xenografts were allowed to grow, and mice were then randomly split into two groups. Animals in first group were treated daily for 5 days with 200 μL dabrafenib (25 mg/kg) plus trametinib (2.5 mg/kg) via oral gavage (OG) and with an intraperitoneal (IP) injection control (DT treated group). Animals in the second group were given equivalent volumes of OG and IP vehicle controls (VV control group). The vehicle for OG was 0.5% hydroxypropylmethylcellulose, 0.2% Tween 80 in pH 8.0 distilled water. Tumor volume was calculated from daily measurements by caliper (see Figure S5A). After 5 days, mice were transcardially perfused with oxygenated and heparinized Tyrode's solution which allowed for simultaneous euthanasia and exsanguination. Flank xenografts were then surgically removed and fixed in 4% paraformaldehyde (PFA) in PBS and stored at 4 °C for 48 h. All fixed tumors from a single group were uniformly paraffin embedded into a single block holder and sectioned in 5 μm slices.

Xenograft for Live-Cell Intravital Imaging

All animal research was performed in accordance with guidelines from the Institutional Subcommittee on Research Animal Care, and studies related to intravital microscopy were performed under approval of the Institutional Animal Care and Use Committee (IACUC) at Massachusetts General Hospital. Titanium dorsal skin-fold window chambers (APJ Trading) were implanted in 6-10-week-old female nu/nu mice (MGH Cox7), and 2 x 10^6 A375 reporter cells in 50 μl PBS were injected under the fascia. Analgesic buprenorphine was used prior to, and for 3 days after, surgical implantation, which was performed under 2% isoflurane supplied with 2 L/min O2. Window chambers were sealed with sterile coverslips, and mice were supplied prophylactically with drinking water containing antibiotics.

METHOD DETAILS

Construction of CRISPRi and CRISPRa A375 Cell Lines

All lentivirus particles were produced in HEK293T cells transfected with the lentiviral plasmid of interest (as described in relevant sections on cloning). psPAX2 (Addgene #12260) and pCMV-VSV-G (Addgene #8454) were introduced into cells in a 2:2:1 molar ratio using lipofectamine 3000 (Invitrogen) according to the manufacturer's instructions. After 2 days, growth medium containing the lentiviral particles was harvested, centrifuged, filtered through a 0.45 μm low-protein binding membrane and stored at -80°C.

To generate an A375 cell line stably expressing dCas9-KRAB (A375_i), A375 cells were transduced with lentiviral particles produced using vector pMH0001 (Addgene #85969; which expresses dCas9-BFP-KRAB from a spleen focus forming virus (SFFV) promoter with an upstream ubiquitous chromatin opening element) in the presence of 8 μg/mL polybrene (Sigma). A pure polyclonal population of dCas9-KRAB expressing cells was generated by two rounds of fluorescence activated cell sorting (FACS) gated on the top half of BFP positive cells (BD FACS Aria II). The performance of A375_i in knocking down endogenous genes was evaluated by individually targeting 3 control genes (ST3GAL4, SEL1L, DPH1) and measuring gene expression changes by RT-qPCR (dataset provided in Synapse database, see Table S4 and Data availability).

To generate an A375 cell line stably co-expressing dCas9 fused to SunTag, and a SunTag-binding antibody fused to the VP64 transcriptional activator (A375_a), A375 cells were first transduced with lentiviral particles produced using vector pHRdSV40-dCas9-10xGCN4_v4-P2A-BFP (Addgene #60903; expresses dCas9 tagged with 10 copies of the GCN4 peptide v4 and BFP) in the presence of 8 μg/mL polybrene. After selection of BFP positive cells using one round of FACS, cells were transduced with lentiviral particles produced using vector pHRdSV40-scFv-GCN4-sfGFP-VP64-GB1-NLS (Addgene #60904; expresses a single-chain variable fragment that binds to the GCN4 peptide fused to GFP and VP64) in the presence of 8 μg/mL polybrene. Single cells with high GFP levels (top 25% of GFP positive cells) and high BFP levels (top 50% of BFP positive cells) were isolated by FACS. Monoclonal cell lines were expanded and a single clone exhibiting robust growth and robust overexpression of target genes was selected as cell line A375_a. The performance of A375_a in overexpressing endogenous genes was evaluated by individually targeting 3 control genes (CDKN1C, SLC4A1, POU5F1) and measuring gene expression changes by RT-qPCR (dataset provided in Synapse database, see Table S4 and Data availability).

CRISPRi and CRISPRa A375 Cell Lines Targeting EGFR

Pairs of complementary synthetic oligonucleotides (Integrated DNA Technologies) forming sgRNA protospacers flanked by BstXI and BlpI restriction sites were annealed and ligated into BstXI/BlpI double digested plasmid pU6-sgRNA EF1Alpha-puro-T2A-BFP (Addgene #60955). Protospacer sequences used to target individual genes and synthetic oligonucleotides used to build them are listed in Table S2. The sequence of all sgRNA expression vectors was confirmed by Sanger sequencing. Lentivirus particles were produced using these vectors as described earlier.

A375_i and A375_a cells were infected with sgRNA expression vectors by addition of lentivirus supernatant to the culture medium in the presence of 8 μg/mL polybrene. Transduced cells were selected using puromycin (1.0 μg/mL) starting 48 hr post-transduction and over the course of a minimum of 7 days with daily addition of the antibiotic. After 24 hr growth in puromycin-free medium, 1.0^5 cells were harvested and total RNA was extracted using the RNeasy Plus Mini kit (Qiagen). cDNA was synthesized from 0.1 μg total RNA using Superscript IV reverse transcriptase (Invitrogen) and oligo(dT)20 primers (Invitrogen), following the manufacturer's instructions. Reactions were diluted four-fold with water and qPCR was performed in 10 μL reactions in 384-well plates using PowerUp SYBR Green PCR Master mix (ThermoFisher Scientific), 2 μL of diluted cDNA preparation, and 0.4 μM of primers using a QuantStudio 6 real-time PCR system (Applied Biosystems). All qPCR primers are listed in the dataset provided in Synapse database, see Table S4 and Data availability. To calculate changes in expression level of target genes, all gene specific Ct values were first normalized to GAPDH Ct values (ΔCt). Log_2 fold changes in expression were then determined by the difference between the ΔCt value of targeting sgRNAs and that of a non-targeting negative control sgRNA (A375_iNC or A375_aNC) (ΔΔCt).

Generation of Clonal Cell Lines

A375 cells were grown for at least two passages to 80% confluence in a 10 cm dish. Cells were washed with PBS and then incubated with 0.25% trypsin/2.21 mM EDTA (Corning) for 2 min. After adding 20 mL complete medium, cells were thoroughly homogenized into a single cell suspension. Cell count and homogeneity was determined using a TC20 automated cell counter (Bio-Rad). The cell suspension was serially diluted with tissue culture medium cotaining 10% FBS to a final concentration of 20 cells in 15 mL and 150 μL of that dilution was dispensed in wells of a 96-well plate (0.2 cells per well). After about 14 days, wells that showed clonal growth (15-20 per 96-well plate) were expanded by passaging cells into larger dishes in complete medium.

ERK Activity Fluorescent Reporter Cell Line

A375 cells were transfected with plasmids 4_pPB_ERKKTRmTq2_H2BVenus_mCherryGeminin (Fallahi-Sichani et al., 2017) and pCMV_hyPBase (Fallahi-Sichani et al., 2017) at a 5:2 ratio (w/w) using lipofectamine 3000 according to the manufacturer's instructions. Transfected cells were selected using puromycin (1 μg/mL) starting 48 hr after transfection and over the course of 7 days. A polyclonal population of cells expressing all 3 fluorescent proteins (mturquoise2, Venus and mCherry) was subsequently generated by two rounds of FACS (BD FACS Aria II).

Drugs and Growth Factors

The following chemicals from MedChem Express were dissolved in dimethyl sulfoxide (DMSO) at 10 mM: vemurafenib, dabrafenib, PLX8394, AZ628, LY3009120, cobimetinib, trametinib, selumetinib, binimetinib, PD0325901, lapatinib, erlotinib, SHP099, R248, infingratinib. The following ligands were from Peprotech (catalogue number): EGF (100-15), NRG1 (100-03), FGF8 (100-25A), HGF (100-39). All ligands were prepared in media supplemented with 0.1% bovine serum albumin.

Immunofluorescence Staining, Quantitation, and Analysis for Cell Cultures

The following primary and conjugated antibodies with specified vendor, animal sources and catalogue numbers were used in immunofluorescence analysis of cells and tissues at the specified dilution ratios: p-ERKT202/Y204 rabbit mAb (Cell Signaling Technology, clone D13.14.4E, Cat# 4370), 1:800; p-MEKS217/221 rabbit mAb (Cell Signaling Technology, Cat# 9121), 1:200; p90RSKT359 rabbit mAb (Cell Signaling Technology, D1E9, Cat# 8753), 1:400; EGFR mouse mAb (Thermo Fisher, 199.12, Cat# MA5-13319), 1:100; Axl Rabbit mAb (Cell Signaling Technology, Cat#8661), 1:100; cMet Rabbit mAb (Cell Signaling Technology, Cat#); c-Met (D1C2) Rabbit mAb (Cell Signaling Technology, Cat#8198), 1:100; phospho-γH2AX (Ser139) rabbit mAB (Cell Signaling Technology, Cat# 9718), 1:400; pS6S240/S244 Alexa Fluor 488 Conjugate rabbit mAb (Cell Signaling Technology, D68F8, Cat# 5018), 1:800; pS6S235/S236 Alexa Fluor 555 Conjugate rabbit mAb (Cell Signaling Technology, D57.2.2E, Cat# 3985), 1:400. Immunofluorescence assays for cultured cells were performed using cells seeded in either 96-well plates (Corning Cat#3603) or 384-well plates (CellCarrier Cat#6007558) for 24 hr and then treated with compounds or ligands either using a Hewlett-Packard D300 Digital Dispenser or by manual dispensing.

Cells were fixed in 4% PFA for 30 min at room temperature (RT) and washed with PBS with 0.1% Tween-20 (Sigma) (PBS-T), permeabilized in methanol for 10 min at RT, rewashed with PBS-T, and blocked in Odyssey blocking buffer (OBB LI-COR Cat. No. 927401) for 1 hr at RT. Cells were incubated overnight at 4 °C with primary antibodies in OBB. Cells were then stained with rabbit and/or with mouse secondary antibodies from Molecular Probes (Invitrogen) labeled with Alexa Fluor 647 (Cat# A31573) or Alexa Fluor 488 (Cat# A21202) both at 1:2000 dilution. Cells were washed with PBS-T and then PBS and were next incubated in 250 ng/mL Hoechst 33342 and 1:2000 HCS CellMask™ Blue Stain solution (Thermo Scientific) for 20 min. Cells were washed twice with PBS and imaged with a 10× objective using a PerkinElmer Operetta High Content Imaging System. 9–11 sites were imaged in each well for 96-well plates and 4-6 sites for 384-well plates.

Image segmentation, analysis, and signal intensity quantitation were performed using the Columbus software (PerkinElmer). Cytosol and nuclear areas were identified by using two different thresholds on the CellMask™ Blue Stain (low intensity) and Hoechst channels (~100-fold more intense) and cell boundaries were used to define membrane (2 pixels surrounding cytosolic area), cytosolic and nuclear cell masks. Cells were identified and enumerated according to successful nuclear segmentation. Apart when otherwise specified, immunofluorescence quantifications are average signals of the cytosolic area. Population average and single cell data were analyzed using custom MATLAB 2017a code. Single cell density scatter plots were generated using signal intensities for individual cells.

EdU Incorporation Experiments

Prior to immunofluorescence staining (as above), cells were pulsed for 3 hr with EdU (Lumiprobe, Hunt Valley, MD). After fixing, antibody staining and image segmentation, DNA content was quantified by using the total Hoechst intensity within the nuclear mask and EdU incorporation was quantified by the average intensity within the nuclear mask. The threshold for identification of EdU positive cells was determined by evaluating DMSO control cells (Edu intensity of 300 a.u.).

Immunofluorescence Staining, Quantitation, and Analysis of FFPE Xenograft Tissue Slides

Dewaxing, antigen retrieval and staining of FFPE samples was performed as previously described (Lin et al., 2018) with the following modifications. Samples were subjected to three rounds of photochemical bleaching, then stained with Hoechst 33342 (2 μg/mL) in OBB and antibodies against p-ERK (1:200, Cell Signaling Technologies, Cat. No. 4370S), then anti-rabbit IgG (1:2000, Thermo Fisher, Cat. No. A31573) and finally S100 (1:200, Abcam, ab207367), p-S6 (1:100, Cell Signaling Technologies, Cat. No. 3985S). Slides were imaged using a CyteFinder fluorescence microscope (RareCyte) with 10× (NA=0.3) and 40× (NA=0.6) objectives. We generated whole tumor images from image tiles using Ashlar, a software tool that performs simultaneous stitching and registration of cyclic microscopy images of large tissue sections (https://github.com/labsyspharm/ashlar). We combined Ilastik1.3.2 (Sommer et al., 2011) and CellProfiler3.1.8 (Lamprecht et al., 2007) to enable robust single cell segmentation across all xenograft samples. We used random forest classification implemented in Ilastik to train three distinct classes (nuclei, membrane, and background) to create probability maps for each class. Large images were divided into two images (left and right) to improve performance. Subsequently, CellProfiler was used to segment those probability maps to create labeled single cell masks. Intensity of pERK and S100 staining was quantified within the cellular masks and CSV files were created for downstream analysis using histoCAT (Schapiro et al., 2017) (https://github.com/BodenmillerGroup/histoCAT).

Intravital Live-Cell Microscopy

Upon tumor formation 1-2 weeks post-implantation, subjects were imaged on a FluoView FV1000MPE confocal imaging system (Olympus America). Images were acquired with a XLFluor 2x air objective (NA=0.14, Olympus) or a XLUMPLFLN 20x water immersion objective (NA=1.0, Olympus), with 1-4x digital zoom. Fluorescence channels were sequentially excited with an Argon-ion laser at

458 nm and 515 nm and with a diode laser at 559 nm using a DM 404-458/515/559-561 dichroic beam splitter. CFP emission light was collected using a SDM510 dichroic beam splitter and a BA480-495 filter, YFP with a SDM560 and a BA535-565 filter, and mCherry using a BA575-675 filter. In treated subjects, 25 mg/kg dabrafenib and 2.5 mg/kg trametinib (both from LC labs) were given by oral gavage in water with 1% DMSO and 0.5% methylcellulose, 48 hr and again 24 hr prior to the imaging session. On the day of the imaging experiment, the mice were anesthetized by isoflurane, mounted on a heated microscope stage (37 °C), and continually monitored for stable respiration. Each time-lapse imaging session was performed by (a) using 2x images to identify >3 representative tumor regions for imaging at higher 20x magnification, (b) programming the microscope stage to acquire confocal z-stacks at each position, typically with z-slices at 5 μm depth intervals, and (c) imaging each selected tumor region at roughly 5 min intervals, for a duration of up to 6 hr.

Western Blot Staining, Quantitation, and Analysis

Cells were harvested at 70-80% confluence and lysates were prepared by incubation in Laemmli Sample Buffer (Bio-Rad, #1610737) for 5 min at 95 °C. Lysates were subjected to SDS-PAGE using 4-20% polyacrylamide gels (Bio-Rad, #456-9036). After transfer onto nitrocellulose, proteins were detected using primary antibodies from Cell Signaling (EGFR, #4267, 1:1000) and Santa Cruz Biotechnology (Actin-HRP, #sc-47778 HRP, 1:5,000) and secondary HRP-conjugated antibodies from Cell Signaling (#7074 and #7076, 1:10,000). HRP was detected using ECL substrate purchased from Thermo Scientific (#34076) using a myECL Imager, and signals were quantified using the Image Studio Lite software (LI-COR Biosciences) by normalizing the specific signal for each sample to the Actin signal.

Receptor Quantification by Luminex Bead-Based ELISA

Absolute receptor abundances for EGFR, Her2, Her3 and c-Met were quantified using a Luminex bead-based ELISA procedure as previously described (Claas et al., 2018). A375 cells were cultured in the presence or absence of vemurafenib (1 μM) for 24 hr and then one of four growth factors (EGF, NRG1, FGF8 and HGF at 100 ng/mL) was added for 24 hr. Cells were lysed in 50 μL NP40 lysis buffer (20 mM Tris–HCl, 150 mM NaCl, 2 mM EDTA, 1% NP40, 10% Glycerol, pH 7.4) at 4 °C and lysates were were clarified by centrifugation for 15 min at ~2300 ×g and stored at - 20 °C prior to use. For Met, EGFR, Her2 and Her3, capture antibodies (MAB3581, AF231, MAB1129, and MAB3481, respectively), biotinylated detection antibodies (BAF358, BAF231, BAF1129, and BAM348, respectively) and recombinant proteins used for quantification (8614-MT, 344-ER, 1129-ER, and 348-RB respectively) were from R&D systems. Streptavidin Phycoerythrin (SAPE) was from Biorad (#171304501).

Capture antibody conjugated beads were generated by incubation of MagPix beads (Luminex Corp.) with 5 mg/mL EDC (N-(3-dimethylaminopropyl)-N'-ethylcarbodiimide, Sigma) and 5 mg/mL S-NHS (N-hydroxysulfosuccinimide, Pierce) in 80 mM NaH2PO4 pH 6.3 for 20 min in the dark at RT. After washing, the beads were incubated with 0.1 mg/mL capture antibody in 50 mM HEPES, pH 7.4 at 4 °C overnight. After washing, beads were stored at 4 °C in PBS + 1% BSA and 1% Tween20. After addition of conjugated beads to wells of a 384-well Optiplate (Perkin Elmer) and washing with assay buffer (PBS + 0.1% BSA and 0.1% Tween20), cell lysate samples were added and incubated overnight at 4 °C with shaking at ~8000 rpm. Samples were diluted if necessary to be in the log-linear range of the standard curve determined with recombinant proteins. After washing, detection antibodies were diluted 1000× in assay buffer and incubated at RT for 1 hr with the sample. After washing, SAPE was diluted 100× in assay buffer, added to wells and incubated at RT for 15 min. After final washing, samples were read on a Flexmap 3D machine (Luminex Corp) according to manufacturer's protocol.

Live-Cell Microscopy

A375 cells expressing the ERK activity fluorescent reporter (see above) were plated on poly-D-lysine-coated glass bottom dishes (MatTek, P35G-0.170-14-C) 48 hr prior to imaging at a density of 30,000 cells per dish. Drugs were added 24 hr before imaging. Time lapse imaging was performed in DMEM without phenol red with 4.5 g/l glucose, L-glutamine, and sodium pyruvate (Corning) and supplemented with 5% FBS. Cells were imaged on a Nikon Eclipse TE-2000 inverted microscope with a 20× plan apo objective (NA 0.7 5) with a CCD camera. The microscope was enclosed with an environmental chamber to maintain humidity, a temperature of 37°C and 5% CO2. Images were captured in CFP, YFP and Texas Red channels every 6 min using the MetaMorph software (Molecular Devices). The filter sets used were as follows: CFP– 436/20nm, 455nm, 480/40nm (excitation filter, beam splitter, emission filter); YFP – 500/20nm, 515 nm, 520nm; Texas Red – 560/40nm, 585nm, 630/75nm; All filters were obtained from Chroma. Cell tracking and data analysis was performed using MATLAB scripts (Cappell et al., 2016; Reyes et al., 2018).

Note on the Validity of Using the ERK:KTR Live-Cell Reporter to Assay Kinase Activity at Different Cell-Cycle Phases

In the course of this work we identified a potential complication with the ERK:KTR live-cell reporter even though it is widely used (Regot et al., 2014). We noticed that traces from single cells expressing ERK:KTR suggested that ERK becomes active in all S/G2 phases even when RAF or MEK inhibitors are present at high levels just before cells become Geminin positive (see end of traces in Figure 2C; in Videos S2 and S3). We did not observe ERK activity under these conditions using immunofluorescence staining and ERK:KTR translocation in S/G2 was unaffected by saturating doses of MEK or ERK inhibitors. We speculate that the ERK:KTR reporter can be activated in S/G2 phases by a CDK (e.g. CDK2) because the reporter contains a sequence similar to a degenerate CDK2 substrate motif. Phosphorylation at this site would result in modification of one of the two phosphosites controlling ERK:KTR nuclear-to-cytosolic translocation. If this is correct similar problems may affect other KTR reporters having the same backbone; these include the JNK and p38 KTR reporters (Regot et al., 2014) and the more recently described CDK4 KTR reporter (Yang et al., 2020).

In this paper we collect ERK:KTR activity data only from A375 cells in G0/G1. We accomplished this by pre-treating A375 cells for 24 hours with RAF or RAF plus MEK inhibitors prior to the start of live-cell imaging. We ignored data from cells that were Geminin positive at start of imaging. As observed in a comparison of Figures 1A–1C with Figure 1H, ERK:KTR activity and pERK levels by immunofluorescence are very similar in G0/G1 cells. More specifically, we confirm a correspondence between ERK:KTR activity and anti-pERK immunofluorescence in: i) untreated A375 cells with active oncogenic signaling; ii) in the distribution of ERK activity in cells treated with RAF inhibitors (when ERK positivity is restricted to a small subset of pulsing cells); iii) the spatial distribution of pulsing cells with and without added growth factors; (iv) when MEK inhibitors are used at concentrations above 1 μM and above to suppress all ERK activity. We are therefore confident that the ERK:KTR traces for cells in G0/G1 phases as reported in this paper accurately reflect ERK activity.

Targeted Proteomics Quantification of Protein Abundance and Phosphorylation

Targeted quantification of protein abundances and phosphorylation was performed as previously described (Shi et al., 2016). Briefly, cell pellets from A375 cell lines treated with different doses of vemurafenib were lysed in 100 μL of lysis buffer containing 8 M urea in 100 mM NH4HCO3 (pH 7.8). Proteins were reduced by 5 mM dithiothreitol for 1 hr at 37 °C and alkylated using 20 mM iodoacetamide for 1 hour at RT in the dark. Samples were diluted eightfold with 50 mM NH_4HCO_3 and digested by sequencing grade modified trypsin at a 1:50 enzyme-to-protein ratio (w/w) at 37 °C for 3 hr. Each sample was then desalted by C18 solid phase extraction and concentrated to ~100 μL. The final peptide concentration was measured using bicinchoninic acid assay with an average of ~4 μg/μL. 10 μg and 100 μg of the peptide mixture per sample were used with the addition of 200 fmol and 50,000 fmol of crude heavy peptides for quantification of protein abundance and protein phosphorylation dynamics, respectively.

For protein abundance quantification (Shi et al., 2016)(Yi et al., 2018), crude heavy-isotope labeled synthetic peptides were purchased from Thermo Scientific and the two best response peptides were selected to configure final selected reaction monitoring (SRM) assays for each target protein. All samples were measured by regular LC-SRM using the scheduled SRM algorithm (Shi et al., 2017) for simultaneous quantification of the selected target proteins. For targeted quantification of phosphorylation (Yi et al., 2018), phosphopeptides were selected for core component proteins for the EGFR-MAPK pathway. Crude heavy-isotope-labeled phosphopeptides were purchased from New England peptides and spiked into the peptide sample prior to phosphopeptide enrichment. Phosphopeptides were enriched by immobilized metal-ion affinity chromatography (IMAC) with Fe3+-NTA agarose beads. Eluted phosphopeptides were dried down and stored at -80 °C until further LC-MS/MS analysis. Lyophilized phosphopeptides were reconstituted in 0.1% FA and subjected to LC-SRM analysis immediately. All LC-SRM measurements were performed using the nanoACQUITY UPLC system coupled online to a TSQ Vantage triple quadrupole mass spectrometer (Thermo Scientific). SRM data were analyzed using Skyline software (MacLean et al., 2010) and the best transitions without interferences were used for quantification. The SRM peak area ratios of the endogenous light peptides over heavy peptide standards (i.e., the L/H ratio) were reported for all SRM measurements. The SRM proteomics data were deposited in the Panorama public database (https://panoramaweb.org/fWeE7i.url).

Transcript Profiling

A375 cells were plated in 24-well plates (Corning, #353047) with 475uL of growth media and allowed to adhere for 24 hours till 50% confluency. Cells were then treated with vemurafenib alone or in combination with cobimetinib and stimulated with EGF (100 ng/mL) at the times indicated by the experimental design. Each condition was performed twice on two different days, for a total of four replicates, two biological with two technical replicates each. Cells were lysed in 96 well plates and RNA was extracted using Applied Biosystems MagMax 96 total RNA isolation kit (Thermo Fisher, # AM1830) with on bead DNase digestion. Sample concentrations were determined by Nanodrop and RNA quality was assessed on a subset of samples by Bioanalyzer (Agilent); all samples scored RINs of > 9.0. RNA sequencing library preparation was performed with the High Throughput TruSeq Stranded mRNA Library Prep Kit (Illumina, # RS-122-2103) following the manufacturer's protocol at half reaction volume. Input for each sample consisted of 500 ng of RNA and 5 μL of 1:500 diluted ERCC spike-in mix 2 (Ambion). Libraries were amplified for 11 cycles during the final amplification step. Libraries were quantified using the Qubit dsDNA HS assay (Thermo Fisher Scientific). Library size and quality were spot checked for a subset of samples by Bioanalyzer (Agilent). The average size of cDNA fragments in the libraries was 330 bp. Libraries were pooled at equimolar concentrations then the pool was quantitated using the KAPA library quantification kit (KAPA Biosystems). Libraries were sequenced single end 75 base pairs using NextSeq500 (Illumina) at the Biopolymer's Facility (Harvard School). For data analysis, RNAseq reads were aligned against GRCh38 human reference using HISAT2 (Kim et al., 2015) in the bcbio framework and gene expression counts in reads per million (RPM) and standard deviations from four replicates were calculated and analyzed with custom MATLAB software. Gene expression data (RNA seq) were deposited in the GEO (Gene Expression Omnibus, https://www.ncbi.nlm.nih.gov/geo/, accession number: GEO: GSE127988).

Estimation of Clinically Accessible Drug Dose Ranges

Clinically accessible drug dose ranges for vemurafenib, dabrafenib, cobimetinib and trametinib were calculated from published concentrations measured in the plasma of human subjects (see Table S3 for values and references).

Model Construction and Definition

MARM1 was built using PySB (Lopez et al., 2013) extended to include support for energy-based BNG (Sekar et al., 2017). Parameters were estimated using AMICI (Fröhlich et al., 2017), pyPESTO (Stapor et al., 2018) and parallelized for cluster computation using

SnakeMake (Köster and Rahmann, 2012). The main model features are explained in the main text and a detailed description of model construction and parameter estimation procedures is provided in Data S1.

Estimation of Receptor-Driven ERK Signaling from Immunofluorescence Data or Modelling

We calculated the net contribution of receptor-driven ERK signaling to MAPK activation by subtracting unstimulated pERK or pMEK signaling from pERK or pMEK signaling measured in the same conditions but after growth factors stimulation. This was done using immunofluorescence data or model simulations to highlight the distinct contribution of receptor activation to MAPK signaling.